THE JOURNAL OF PHYSICAL CHEMISTRY C
A JOURNAL OF THE AMERICAN CHEMICAL SOCIETY

pubs.acs.org/JPCC

Article

Unusual Electronic Properties of Cellulose Nanocrystals Conjugated to Cobalt Phthalocyanine: Long-Lived Charge Separation and Visible-Light-Driven Photocatalytic Activity

Kazi M. Alam, Pawan Kumar, Narendra Chaulagain, Sheng Zeng, Ankur Goswami, John Garcia, Ehsan Vahidzadeh, Manish L. Bhaiyya, Guy M. Bernard, Sanket Goel, Vladimir K. Michaelis, Alexander E. Kobryn, Sergey Gusarov, and Karthik Shankar*

Cite This: https://doi.org/10.1021/acs.jpcc.2c03531

Read Online

ACCESS | Metrics & More | Article Recommendations | Supporting Information

ABSTRACT: Octacarboxylated cobalt phthalocyanine (CoPc) was covalently conjugated to cellulose nanocrystals (CNCs) by employing an esterification protocol. Solid-state NMR, X-ray photoelectron spectroscopy (XPS), Raman, and infrared spectra were used to verify and study the nature of covalent attachment responsible for the immobilization of CoPc on the CNC surface. The covalent attachment was investigated from a theoretical simulation perspective using dispersion-corrected density functional theory (DFT) calculations, which verified the stable bond formation between CNC and CoPc. CoPc is an organic semiconductor with a high exciton binding energy, and CNCs are known to be insulating. Yet, Kelvin probe force microscopy (KPFM) indicated charge carrier generation and long-lived charge separation in the CNC−CoPc conjugate compared to pristine CoPc under visible light illumination. Such behavior is more typical of a semiconductor nanocomposite. The CNC−CoPc conjugate exhibited superior performance in the visible-light-driven surface photocatalytic reduction of 4-nitrobenzenethiol (4-NBT) to *p*,*p*′-dimercaptoazobenzene (DMAB) and photodegradation of rhodamine B.

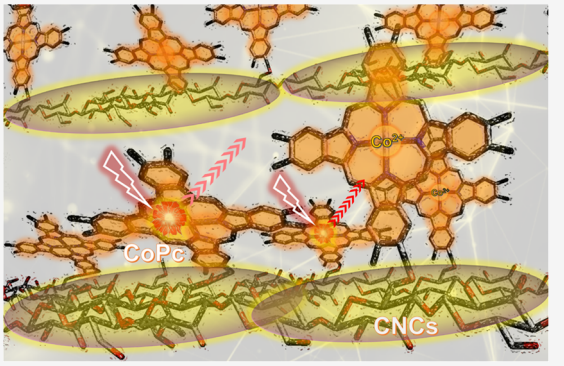

1. INTRODUCTION

Efficient photogenerated charge carrier separation in semiconductor-based photocatalytic systems enhances the performance of solar energy harvesting devices. While this goal has been primarily achieved by constructing semiconductor heterojunctions having appropriate band energetics,[1] achieving such an outcome in semiconductor−insulator heterojunctions is extremely rare.[2] In this work, we report robust photogeneration of charge and unusual long-lived charge separation in a heterosystem comprising semiconducting cobalt phthalocyanine (CoPc) and insulating cellulose nanocrystals (CNCs). Metallophthalocyanine structures with high chemical stability and structural tunability have shown impressive activity in electrocatalytic and photocatalytic reduction reactions either as a standalone catalyst or as a heterosystem coupled with other catalysts.[3−6] Metallophthalocyanines, which have primary applications in the dyeing and printing industry as pigments, are π-conjugated heterocyclic aromatic compounds that have 18 π-electrons delocalized over the molecule.[7] In addition to the applications mentioned above, phthalocyanines have been used as light absorbers and hole transport layers in organic and hybrid photovoltaic devices.[8−10] On the other hand, cellulose is a linear-chain carbohydrate polymer, whose molecular structure renders it important properties such as biodegradability, chirality, hydrophilicity, and wide chemical functionality due to the presence of reactive −OH groups.[11] Cellulose nanocrystals (CNCs) derived from cellulose nanofibrils, following an acid hydrolysis treatment for isolating the crystalline part, are biomacromolecules that form the fundamental building block of a vast number of naturally occurring fiberlike materials in the biosphere.[12] CNCs occupy a leading position in the search for environmentally benign, renewable, biodegradable, biocompatible, and nontoxic raw technological materials. CNCs have a very high elastic modulus, a high aspect ratio, and a low thermal expansion coefficient, which render them suitable for the formation of nanocomposites for reinforcement. CNCs have been used in various technological disciplines, such as food science, pharmaceutical science, energy harvesting, nanomedicine, and

Received: May 21, 2022
Revised: August 24, 2022

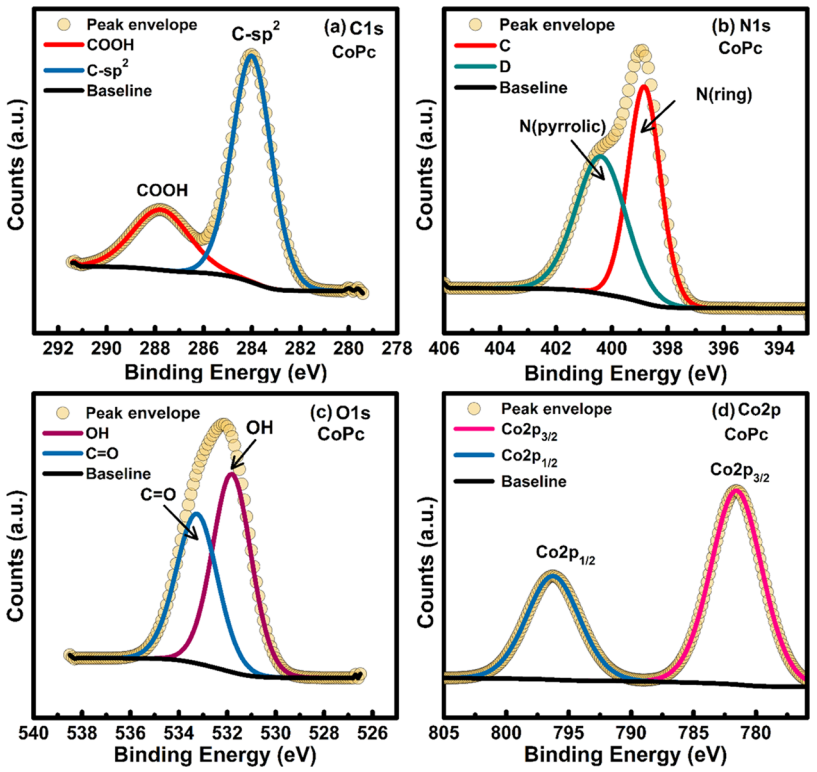

Figure 1. High resolution X-ray photoelectron spectroscopy (HR-XPS) core-level spectra of anodized CoPc (a) in the C 1s region, (b) in the N 1s region, (c) in the O 1s region, and (d) in the Co 2p region.

photonics.[12,13] CNCs have been studied as inactive support matrices or scaffolds for catalysts such as ZnO nanoparticles, mesoporous TiO_2, Fe_3O_4, and Au and Pd nanoparticles.[13,14] Recently a nanohybrid comprising ZnO nanocrystals on melamine formaldehyde-coated CNCs demonstrated a 4-fold increase in photocatalytic activity in the realization of an excellent UV filter.[15] Cellulose nanocrystals have also been employed as morphology modifiers in blended films with conjugated polymers to enhance electrical conductivity and carrier mobility.[16−19]

There are quite a few porphyrin- and phthalocyanine-based catalysts reported in the current literature, but a cellulose-supported system, which has the potential to increase the effective surface area of the catalyst by reducing the different aggregation states, is surprisingly scarce.[20−23] Copper−tetrasulfonate phthalocyanine-grafted CNC was reported as a heterogeneous catalyst for the selective aerobic oxidation of alcohols and alkyl arenes,[20] where the grafting protocol did not involve covalent attachment but rather employed a more common route, namely, magnetic stirring. Tetraamino cobalt phthalocyanine was conjugated with cellulose through aldehyde groups created on the cellulose surface.[22,23] Covalent immobilization of cobalt phthalocyanine (CoPc) onto cellulose was reported by Shaabani et al. by introducing a slightly modified route, where cellulose tosylate was prepared as an intermediate product prior to the covalent attachment.[21] Here, we synthesized octacarboxylated CoPc-conjugated CNC by avoiding any further modification of CNC surface chemistry, instead of taking advantage of the abundant surface −OH groups directly. The novel conjugation protocol involved ester bond formation between CoPc and CNC. Recently, we reported such covalent attachment between octacarboxylated ZnPc and CNC, which demonstrated superior performance in sensing applications through higher photoluminescence (PL) quenching capabilities compared to standalone ZnPc.[24] Additionally, this novel CNC−ZnPc conjugate demonstrated promising electrical bistability, which could be exploited in memory applications.[25] In this work, we tested the synthesized pristine octacarboxylated CoPc and CNC−CoPc conjugates for the photocatalytic transformation of 4-NBT to *p*,*p*′-dimercaptoazobenzene (DMAB) and rhodamine B (RhB) degradation. While the first application was realized by attaching lab-grown Ag nanoparticles, the latter application involved pristine CoPc and the conjugate without Ag. The hybrid systems comprising semiconductors and plasmonic metals are promising in solar energy harvesting applications, as they have complementary optical attributes. In semiconductors, excitons are generated, which are bound electron−hole pairs that evolve following transitions between valence and conduction band energy levels, while on the metal surface, plasmons or collective oscillations of conduction band electrons are the fundamental optical excitations.[26,27] Semiconductors are capable of generating long-lived charge carriers, whereas plasmonic systems can be utilized for generating short-lived hot carriers and concentrating electromagnetic energy through local field amplification.[26] Hence, a synergistic enhancement of photocatalytic performance can be realized in the exciton−plasmon-coupled systems. Experimental and theoretical findings indicated remarkable modification of electronic properties in the CNC−CoPc conjugate with respect to bare CoPc, conducive for optoelectronic applications. Both of these novel conjugates, CNC−ZnPc in our recently reported works[24,25] and CNC−CoPc in the present work, showed promising technological applications in diverse fields such as chemical sensing, electrical memory, and photocatalytic solar energy harvesting. Thus, such success is

https://doi.org/10.1021/acs.jpcc.2c03531
J. Phys. Chem. C XXXX, XXX, XXX−XXX

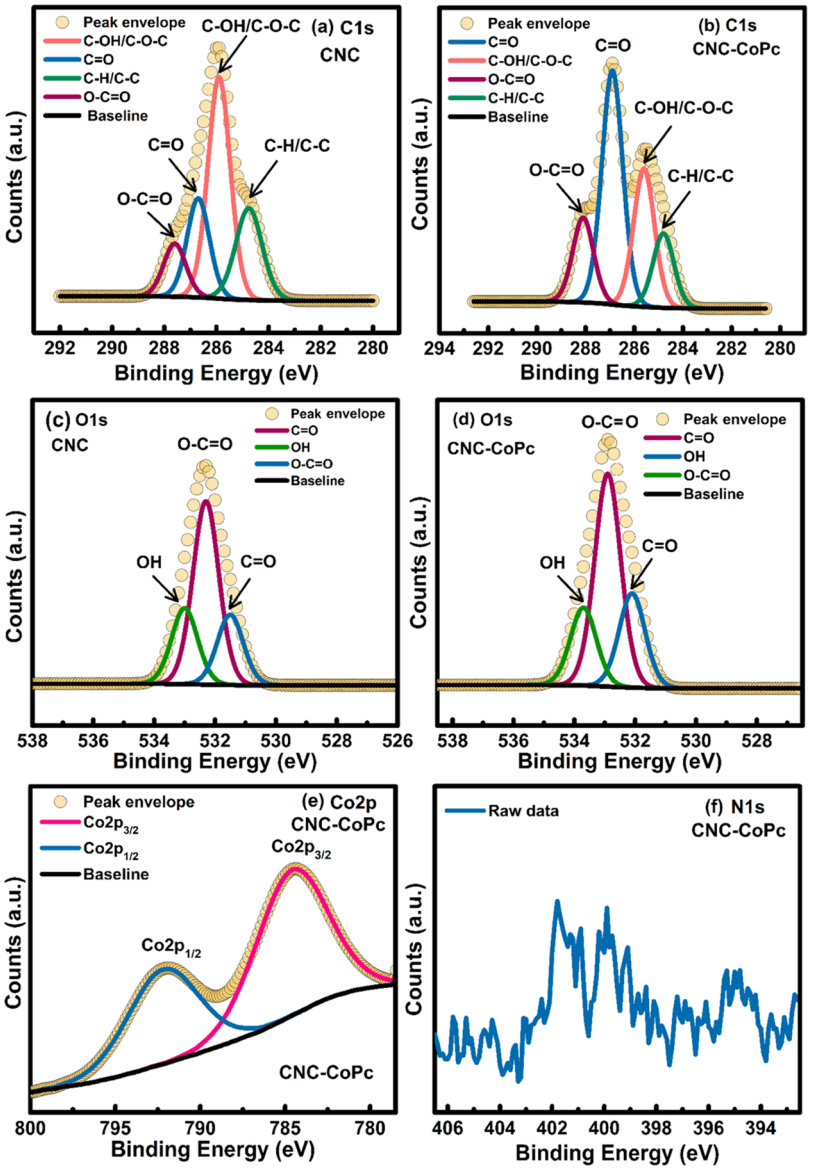

Figure 2. HR-XPS core-level spectra of (a) CNCs in the C 1s region, (b) CNC−CoPc in the C 1s region, (c) CNC in the O 1s region, (d) CNC−CoPc in the O 1s region, (e) CNC−CoPc in the Co 2p region, and (f) CNC−CoPc in the N 1s region.

inevitably expected to promote this novel attachment protocol of cellulose nanocrystals with other phthalocyanines and porphyrins in future scientific endeavors. Moreover, this concept can be easily upscaled. Phthalocyanines are popular textile dyes that are produced in industrial quantities every year. Cellulose nanocrystals are a product of the hydrolysis of wood pulp, hemp, and other biomaterials and are also available in relatively large quantities. In addition, the esterification chemistry used to covalently bind the cellulose nanocrystals to phthalocyanines is widely used in industrial organic synthesis.

2. RESULTS AND DISCUSSION

2.1. Structural and Physicochemical Properties. The details of the esterification protocol used to covalently conjugate CoPc molecules to the surface of CNCs are provided in the synthesis part of the Supporting Information. Sulfuric acid-hydrolyzed CNCs were obtained from Alberta Innovates/Innotech. Note that sulfuric acid-hydrolyzed CNC surfaces have some sulfate groups in addition to the abundance of −OH groups.[28] Figure S1 in the Supporting Information schematically presents the formation of the ester bond between CoPc and CNC involving the −OH groups on the CNC surface. As mentioned in the Supporting Information, we intended to covalently attach a certain amount of CoPc onto the CNC surface (20 wt %) prior to the start of the relevant chemical reactions. However, we pursued atomic absorption spectroscopy (AAS) to determine the actual weight ratio of CoPc and CNC in the CNC−CoPc blend. First, we obtained Co concentration values from known prepared aqueous CoPc and CNC−CoPc solutions, where the concentration was kept the same. Note that, due to the presence of −COOH groups in the former and both −OH and −COOH groups in the latter, both bare octacarboxylated CoPc and the CNC−CoPc conjugate have moderate water solubility. The obtained Co concentration values using the calibration carves were 15.03 and 3.61 ppm for bare CoPc and CNC−CoPc samples, respectively. Thus, the weight percentage of CoPc in the conjugate is 19.37%, which is very close to the intended

https://doi.org/10.1021/acs.jpcc.2c03531
J. Phys. Chem. C XXXX, XXX, XXX−XXX

amount mentioned earlier. The oxidation state, nature of the chemical species, and their binding energies (BEs) were determined using X-ray photoelectron spectroscopy (XPS) (Figures 1, 2, and S2 in the Supporting Information). An XPS elemental survey scan of CoPc displayed peaks corresponding to C 1s, N 1s, O 1s, and Co 2p indicating the presence of all of the constituent elements, while a survey scan of CNC and CNC−CoPc showed the presence of C 1s and O 1s peaks composing the framework of CNCs. Additional peaks corresponding to cobalt (Co 2p and Co 3s) in CNC−CoPc and sulfur (S 2p) on the surface of CNCs were observed in the survey scan. Sulfur was introduced into CNCs during the acid hydrolysis process using sulfuric acid (Figure S2, Supporting Information).

Core-level high-resolution XPS spectra of CoPc in the C 1s region were deconvoluted into two peak components located at BE ≈ 284.02 and 287.8 eV, corresponding to sp^2 hybridized carbons in the conjugated system of phthalocyanine with COOH groups at the periphery. The calculated ratio of contributions from sp^2 hybridized carbons and COOH carbons was ∼2.33:1, which was slightly lower than the theoretical ratio of sp^2 and COOH carbons in octacarboxyphthalocyanine (4:1) and demonstrates a contribution from adventitious carbon to the COOH component (Figure 1a). Deconvoluted HR-XPS spectra in the N 1s region displaying two peak components centered at 398.8 and 400.4 eV were assigned to ring nitrogens (N_{ring}) connecting pyrrole moieties and nitrogen atoms composing pyrrole rings ($N_{pyrrolic}$), respectively.[29−31] The ratio of N_{ring} to $N_{pyrrolic}$ ($N_{ring}/N_{pyrrolic}$) was 50.56/40.44 (∼1:1), which matched well with the phthalocyanine skeleton, again signifying the successful synthesis of the phthalocyanine framework (Figure 1b). Two peak components of approximately equal contributions in the O 1s region at binding energies of 531.8 and 533.2 eV originated due to −OH- and C═O-type oxygens of COOH in octacarboxyphthalocyanine, respectively (Figure 1c).[32] HR-XPS in the Co 2p region gave two peak components at binding energies of 781.5 and 796.35 eV, assigned to Co $2p_{3/2}$ and Co $2p_{1/2}$ peak components of the Co^{2+} state, respectively, confirming that Co was present in 2+ oxidation state (Figure 1d).[33,34]

After deconvolution, the HR-XPS spectra of CNCs in the C 1s region gave four peak components centered at BE ≈ 284.8, 285.8, 286.7, and 287.5 eV, which were assigned to C−H/C−C, C−OH/C−O−C, C═O, and O-C═O carbons present in cellulose polymer, respectively, which is composed of D-glucose units connected with β 1−4 glycosidic linkage (Figure 2a).[35−37] Subsequent to chemical immobilization of CoPc on CNCs *via* ester bond (−COO−) formation between −OH groups on CNCs and activated acyl chloride (COCl) on phthalocyanine, the contribution from the −OH/COC peak at BE ≈ 285.6 eV was reduced significantly, demonstrating that −OH groups were consumed in ester linkage formation (Figure 2b). Additionally, the peak intensity at 286.9 and 288.1 eV due to C═O and O-C═O increased, which confirmed the successful grafting of CoPc on CNCs via ester bond formation. HR-XPS spectra of CNCs in the O 1s region showed three peak components for C═O, O−C═O, and −OH oxygens at BE ≈ 531.4, 532.3, and 532.9 eV, respectively (Figure 2c).[32] After immobilization of CoPc, the peak component corresponding to C═O was increased, while the peak component related to −OH was decreased, which demonstrates that −OH groups were used in ester bond formation (Figure 2d). HR-XPS spectra of CNC−CoPc in the Co 2p region gave two peak components centered at 784.3 and 792.5 eV, confirming the presence of Co^{2+}-containing phthalocyanine (Figure 2e). However, the Co 2p peaks were shifted slightly which was attributed to partial charge transfer from OH groups to Co^{2+} via weak coordination and monolayer coverage.[38] Further, the peak related to N 1s was absent in CNC, showing the absence of nitrogen atoms, while HR-XPS of CNC−CoPc yielded very poor signals which might be due to lower concentration of CoPc and suppression of some signals (Figure 2f). Additionally, S 2p XPS spectra of both CNC and CNC−CoPc peak components assigned to S $2p_{3/2}$ and S $2p_{1/2}$ at 168.2 and 169.5 eV, respectively, revealed the presence of sulfur in the form of sulfate groups (Figure S2c,d, Supporting Information).

The nature of chemical bonding in CoPc, CNC, and CNC−CoPc was studied by solid-state nuclear magnetic resonance (NMR) spectroscopy using the cross-polarization magic-angle spinning (CPMAS) technique (Figure S3a in the Supporting Information). The ^{13}C CPMAS NMR spectra of CoPc exhibited a broad peak in the 125−150 ppm region, attributed to the aromatic carbons of the four isoindole units linked together with N atoms in the aromatic phthalocyanine structure, and a peak at 170 ppm that was assigned to peripheral carboxylic carbons of octacarboxyphthalocyanine units (bottom panel of Figure S3a in the Supporting Information). The ^{13}C CPMAS NMR spectrum of pristine CNC displayed the characteristic resonances for the corresponding C1 (∼105 ppm), C4 (89−85 ppm), C2,3,5 (75−73 ppm), and C6 (∼66 ppm) due to the presence of unique carbons in the D-glucose monomer units linked together with $\beta(1 \rightarrow 4)$-glycosidic linkage (middle panel of Figure S3a in the Supporting Information) and being consistent with cellulose I.[39−42] After chemical functionalization of CNC with CoPc, the ^{13}C NMR signal of CNC (top panel of Figure S3a in the Supporting Information) did not change significantly, with only minor changes in the intensity that can be attributed to CP efficiency and crystallinity, which is consistent with the X-ray diffraction (XRD) results (Figure S3b in the Supporting Information). This further confirms that the bulk nanostructured CNC remains unchanged during the functionalization treatment applied here. Unfortunately, due to the low loading of CoPc and ^{13}C being 1.1% abundant, we cannot detect the aromatic or carboxylic acid resonances of the functionalized CNC. Finally, the low-intensity residual ^{13}C resonances at 165 ppm and between 35 and 40 ppm are attributed to the residual intercalated dimethylformamide (DMF) used for the synthesis of the CNC−CoPc conjugate.

The XRD patterns of pristine CoPc, pristine CNC, and CoPc-grafted CNC are displayed in Figure S3b in the Supporting Information. The diffraction peaks at 15.2, 16.7, 22.6, and 34.7° (middle panel of Figure S3b in the Supporting Information) are the manifestations of reflections from $(1\bar{1}0)$, (110), (200), and (040) planes of cellulose I, respectively.[43,44] All of these peaks are found in the CNC−CoPc conjugate as well, with almost unchanged features (top panel of Figure S3b in the Supporting Information). An intensity increase was found for the (040) plane. The X-ray diffractogram for bare CoPc showed high crystallinity, specifically at 2θ values of 31.7 and 45.5°. Thus, octacarboxylated CoPc is characterized by its polycrystalline nature, unlike amorphous CoPc.[45] The two most intense peaks at 7.3 and 25.9° of CoPc are present in the CNC−CoPc conjugate, albeit with lower intensities, probably due to the presence of a few layers of stacked CoPc on the

https://doi.org/10.1021/acs.jpcc.2c03531
J. Phys. Chem. C XXXX, XXX, XXX−XXX

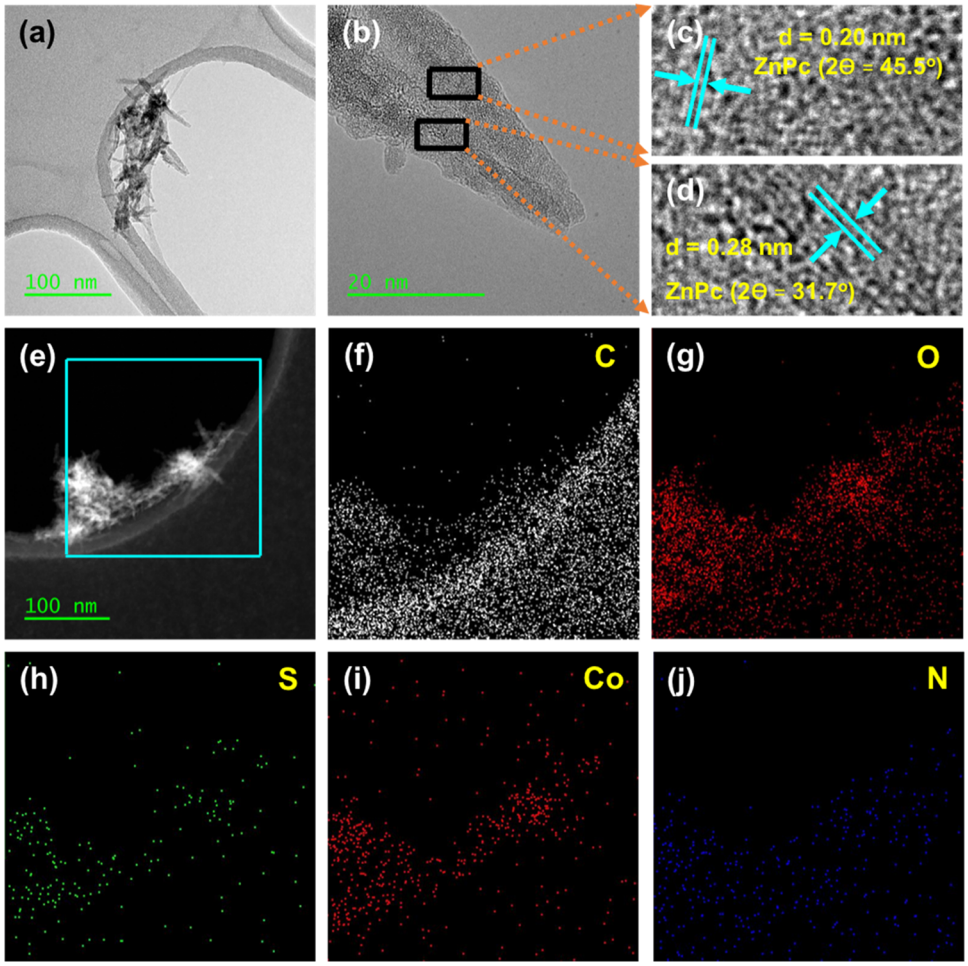

Figure 3. (a) TEM image of an agglomeration of CoPc-conjugated CNCs. (b) HRTEM image of CNC−CoPc. (c), (d) Selected magnified regions of (b) showing lattice planes of CoPc attached on the CNC surface. (e) Dark-field STEM-EDX image of a cluster of CoPc-conjugated CNCs. STEM-EDX elemental mapping images for (f) C, (g) O, (h) S, (i) Co, and (j) N.

CNC surface. The XRD results confirmed the successful grafting of CoPc on the CNC surface.

Fine structural features were determined from high-resolution transmission electron microscopy (HRTEM) images. Figure 3a shows a low-magnification TEM image, showing a bundle of CoPc-conjugated CNCs. HRTEM images of a few CNC−CoPc nanorods can be seen in Figure 3b−d, where panels (c) and (d) are selected magnified regions of panel (b). The lattice fringes (d-spacings) were found to be 0.20 nm and 0.28 nm, respectively, corresponding to XRD peaks at 2θ values of 45.5 and 31.7° for CoPc (Figure S3b in the Supporting Information). These figures indicate complete wrapping of CoPc around CNC nanorods. In other words, the conjugated CNC−CoPc nanorods seem to have core−shell morphology with a CNC core and a shell of aggregated CoPc molecules. Thus, the amount of CoPc covalently grafted onto the CNC surface has a limit. However, in this case, there was a good agreement between our intended CoPc amount and the AAS revealed amount discussed earlier. It would be interesting to investigate such a limit, which is beyond the scope of this current work. The elemental maps collected in scanning transmission electron microscopy (STEM) mode based on energy-dispersive X-ray (EDX) imaging are shown in Figure 3e−j. These figures show the presence of constituent elements from CNC and CoPc and attest to the successful conjugation between CNC and CoPc.

The vibrational properties were studied by Raman and Fourier transform infrared (FTIR) spectroscopy for pristine CNC, pristine CoPc, and CNC−CoPc. Raman spectra show a characteristic fingerprint peak for CNC at 1098 cm^{-1} (middle panel of Figure S4a in the Supporting Information) that arises due to the C−O−C stretching modes in cellulose.[46,47] This vibrational signature is present in the CoPc-conjugated CNC as well, demonstrating the successful attachment between the two systems (top panel of Figure S4a in the Supporting Information). Figure S4a (bottom panel, Supporting Information) shows the Raman spectra of bare CoPc. Metal phthalocyanine vibrations are broadly categorized into low- and high-frequency bands. Lower-frequency vibrations are mainly vibrations of macrocycles and metal−nitrogen bonds, while higher-frequency vibrations involve macrocycle-modified motion of isoindole rings.[48] All of the fingerprint peaks of metallophthalocyanine rings in both the low- and high-frequency regions are present (Figure S4a, bottom panel, Supporting Information).[48−52] The Raman peaks at 673 and 743 cm^{-1} are the two most sharp and narrow vibrational signatures in the low-frequency range that correspond to coupled macrocycle-pyrrolic modes and out-of-phase deformation of the isoindole groups, respectively.[48,50,52] A reduction in

https://doi.org/10.1021/acs.jpcc.2c03531
J. Phys. Chem. C XXXX, XXX, XXX−XXX

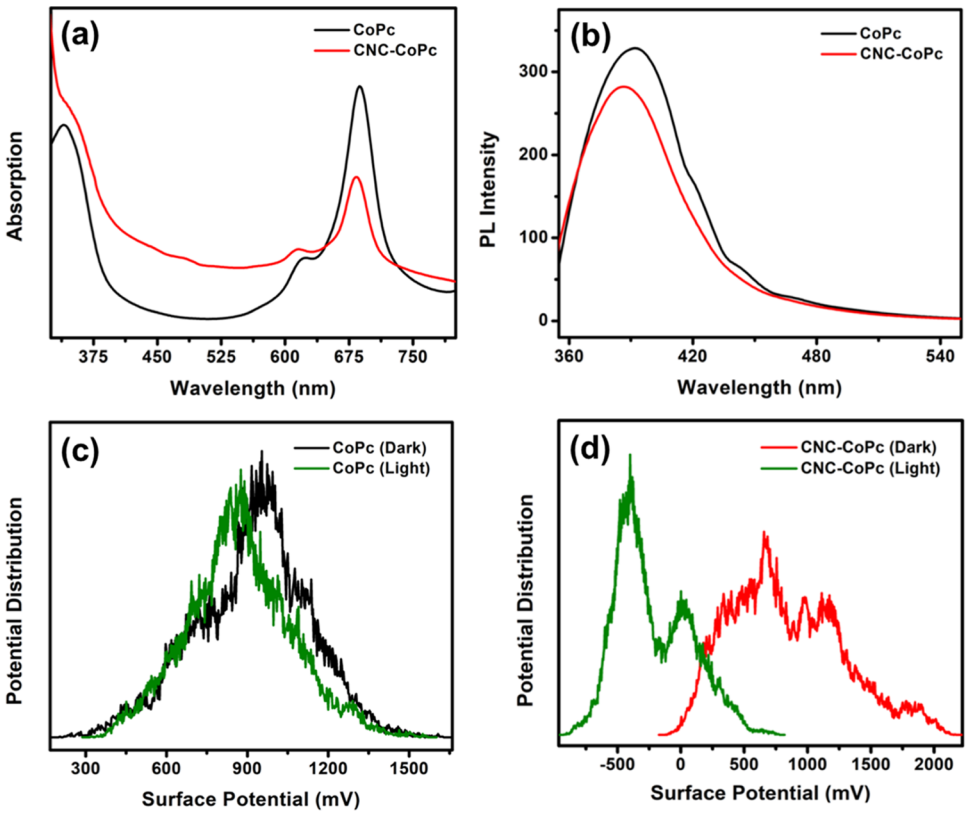

Figure 4. (a) UV−vis spectra of CoPc and CNC−CoPc. (b) Soret band emission spectra of CoPc and CNC−CoPc at 340 nm excitation wavelength. All of the absorption and photoluminescence data were collected in DMF. Kelvin probe force microscopy (KPFM) surface potential distribution in the dark and under illumination conditions (LED 635 nm) for (c) pristine CoPc and (d) CNC−CoPc.

the intensity of the peak at 673 cm^{-1} in the CNC−CoPc compared to that for pristine CoPc implies a structure that is slightly distorted from a square-planar configuration, as a result of binding of CoPc on the CNC surface through covalent attachment.[48] In the high-frequency region, peaks at 1321 and 1532 cm^{-1} represent symmetric vibrations of Co−N coupled with indole and benzene ring deformations and out-of-phase stretching of C−N−C bridges due to a symmetric motion of four isoindole groups, respectively.[48,50,52] No noticeable reduction in the intensity was observed for these two CoPc Raman peaks upon conjugation with CNC. However, there is a significant attenuation of the peak at 1438 cm^{-1} in the CNC−CoPc, which corresponds to deformation of the isoindole ring system.[48] A significant opposite behavior is observed for the vibration at 1209 cm^{-1} that involves isoindole ring stretch. This peak, which is pronounced in the conjugate, corresponds to the vibration of phthalocyanine, characterized by a displacement directly along C−C bonds, and consequently affects the macrocycle in an asymmetric fashion.[48] Thus, the strongly modified vibrational features in both lower- and higher-frequency regions for the CNC−CoPc system confirm the successful conjugation.

Fourier transform infrared (FTIR) spectroscopy was employed to characterize the vibrational features of pristine CoPc, pristine CNC, and the conjugate (Figure S4b in Supporting Information). The spectrum for CoPc (bottom panel of Figure S4b in the Supporting Information) shows all of the signature peaks associated with phthalocyanine skeletal vibrations, metal−ligand vibrations, and symmetric (or asymmetric) stretches of metallophthalocyanine.[53−55] The peaks at 721, 1065, and 1134 cm^{-1} were not visible in the CNC−CoPc conjugate, while peaks at 1254, 1392, and 1518 cm^{-1} appeared in the spectrum of the conjugate (top panel of Figure S4b in the Supporting Information). The signature peak of octacarboxylated CoPc appeared at 1685 cm^{-1}, corresponding to the −C═O of the −COOH group.[53] This peak shifted to a lower frequency (1655 cm^{-1}) in the conjugate as a consequence of binding with CNC through an esterification protocol (see the Methodology section in the Supporting Information). Figure S4b (middle panel, Supporting Information) shows the FTIR spectrum of the bare CNC. The characteristic vibrational features of CNC were in complete agreement with the literature.[56] The most noticeable observation from these FTIR plots is the change in the 3000−3500 cm^{-1} spectral range (yellow shaded area in Figure S4b in the Supporting Information). This region represents the −OH stretching vibrations that appear due to an abundance of hydroxyl groups on the CNC surface. The peaks at 3282 and 3331 cm^{-1} (Figure S4b in the Supporting Information) arise due to intermolecular hydrogen bonding and two more peaks of smaller amplitude at slightly higher frequencies (not shown here as they are barely discernible) represent intramolecular hydrogen bonding.[57] The main, broad −OH stretching peak has a significantly reduced intensity in the conjugate compared to that for pristine CNC, indicating a reduction of −OH groups in the former. As mentioned before, the covalent attachment of CoPc with CNC was performed through ester bond formation, which involved the reaction of −OH groups from the CNC surface with the −COOH groups from octacarboxylated CoPc, and therefore, this intensity reduction is expected in CNC−CoPc.[57] Thus, FTIR spectroscopy

https://doi.org/10.1021/acs.jpcc.2c03531
J. Phys. Chem. C XXXX, XXX, XXX−XXX

confirms the successful conjugation of carboxylated CoPc on the CNC surface.

The photophysical properties of bare CoPc and CNC−CoPc in a DMF solvent were studied by UV−vis absorption and steady-state photoluminescence (PL) spectroscopy (Figure 4). The two characteristic bands, known as the B or Soret band and the Q band of metallophthalocyanines, originate from HOMO (π)−LUMO (π^*) transitions and are evident in the 300−400 nm and 600−800 nm spectral regions, respectively.[58−61] Generally, the higher-energy excited states (Soret band) involve deeper π levels and the degree of mixture between these states precludes a traditional one-electron transition picture.[59,60] In addition, the Soret band is associated with an $n-\pi^*$ transition as well.[62] In the CNC−CoPc system, the lower energy peak of the Q doublet is attenuated to ∼50%, while a moderate increase in the absorption peak is observed in the rest of the spectra (Figure 4a). Both peaks in the Q doublet undergo a minor blue shift as a result of the reduced aggregation since aggregation results in a red shift of the spectrum.[63] Indeed, the covalent attachment-induced conjugation is expected to suppress cofacial aggregation of bare CoPc. The significant increase in the absorption for the conjugate in the 400−600 nm spectral range (where phthalocyanines generally do not absorb photons) suggests the possibility of an enhanced intramolecular charge-transfer transition or an impurity level-mediated transition or a combination thereof.[61] Absorption near the lower-energy side of this spectral range also includes $n-\pi^*$-type transitions, involving aza-nitrogen lone pair orbitals.[60] Photoluminescence spectra of the pristine CoPc and CNC−CoPc were collected from dilute solutions in DMF. Figure 4b (also Figure S5a,b in the Supporting Information) shows the Soret band emission spectra for bare CoPc and the conjugate, respectively. Both systems showed the highest emission intensity at 340 nm excitation, which is also the Soret band absorption maximum (Figure 4a) for both materials. As expected, there is a minor blue shift for the PL peaks of the CNC−CoPc conjugate relative to pristine CoPc because of slightly reduced aggregation in the former as mentioned earlier. The PL plots also reveal that the intensity is decreased in the conjugate compared to that for bare CoPc at all of the excitation wavelengths (Figure S5a,b in the Supporting Information) used for this experiment. It is important to note that at all of the excitation wavelengths used, the conjugate has higher absorption than CoPc. This indicates suppressed radiative recombination due to enhanced charge separation (discussed later in detail) in the CNC−CoPc conjugate, which is beneficial for photocatalytic activity. A common trend in excitation-dependent PL peaks is found for both systems; that is, following 340 nm excitation, a reduction in peak intensity occurs with a concomitant red shift. Such excitation-dependent emission properties can be exploited in multicolor imaging. In this work, we did not investigate the details of the origin of this excitation wavelength-dependent emission spectral shift and the attenuation in PL intensity. However, the simultaneous presence of different types of aggregates (such as H and J) can incorporate multiple discrete electronic states and result in excitation-dependent emission modulation in organic systems.[64]

The charge carrier dynamics of CoPc and CNC−CoPc were studied using Kelvin probe force microscopy (KPFM).[65,66] In this experiment, the surface potential was measured, which is defined as the difference between the contact potentials of the atomic force microscopy (AFM) tip and the substrate surface. A change in surface potential was observed when switching the measurement conditions between dark and illumination. A 635 nm LED was used as a light source, which enables high absorption (Q band) of incident photons for the samples studied. In the dark, the surface potential for the CoPc sample demonstrated a peak at ∼950 mV, while the CNC−CoPc conjugate showed this peak at ∼700 mV (Figure 4c,d). Figure S6a,b in the Supporting Information shows the AFM height and phase images of CNC−CoPc substrates on FTO prior to the KPFM measurements, respectively. It is reasonable to assume that CoPc molecules terminate the surface for both samples and determine the surface charge, which ought to result in a similar surface potential value under dark conditions. However, the observed difference in surface potential in the dark between pristine CoPc films and CNC−CoPc films implies a difference in aggregation states and molecular orientations of CoPc in these two samples. Upon illumination with a 635 nm LED, the surface potential values for both systems showed a negative shift. This shift occurs as a consequence of shifting of the quasi-Fermi levels (thus shifting of work functions of the CoPc and CNC−CoPc substrates) in the irradiation condition. The sign of the shift indicates a further accumulation of electrons in both types of samples under illumination. However, the magnitudes of the observed surface potential shifts are vastly different. Bare CoPc samples experience a relatively small ∼50−75 mV shift in the surface potential (Figure 4c), while the CNC−CoPc samples show a dramatic shift of ∼1050 mV (Figure 4d). Since the charge generation capabilities of both types of samples are relatively similar at 630 nm, the enormously high negative shift of the surface potential for the CNC−CoPc system compared to that for bare CoPc indicates long-lived charge separation upon illumination. Furthermore, the CoPc chromophore appears to retain photogenerated electrons and transfer photogenerated holes to CNCs, which is quite unusual. Keep in mind that in photovoltaic devices comprised of bulk heterojunctions of metallophthalocyanines (MPcs) and methanofullerenes (or other electron acceptors), dissociation of the photogenerated exciton MPc involves transfer of the photogenerated electron to C_{60} (or PCBM), while the photogenerated hole is retained in the MPc molecule.[67,68] We surmise that photogenerated holes transferred to CNC from CoPc in CoPc−CNC might protonate sulfate and bound water on the surface of the CNCs, with subsequent stabilization of the protons through a network of hydrogen bonds. Thus, the well-known phenomenon of interfacial hydrogen bonding in CNCs[69] might also be responsible for the observed long-lived charge separation in CoPc−CNC conjugates.

Cyclic voltammetry measurements in aqueous solvents were pursued to investigate the redox properties of bare octacarboxylated CoPc and the CNC−CoPc conjugate. As mentioned before, both of these materials are soluble in water owing to the presence of −COOH and −OH groups on the surface. Figure S7 (Supporting Information) shows the cyclic voltammograms for bare CoPc and the conjugate. In comparison to the earlier reports on CoPc in organic[70−72] and aqueous solvents,[72] the redox peak couples appeared at around −0.9 V (vs Ag/AgCl) can be attributed to the phthalocyanine ring reduction process, while the redox peak couples at around −0.61 V (vs Ag/AgCl) can be associated to phthalocyanine central metal-based electron transfer [Co(III)/Co(II)]. The other middle peak that was attributed to metal-

https://doi.org/10.1021/acs.jpcc.2c03531
J. Phys. Chem. C XXXX, XXX, XXX−XXX

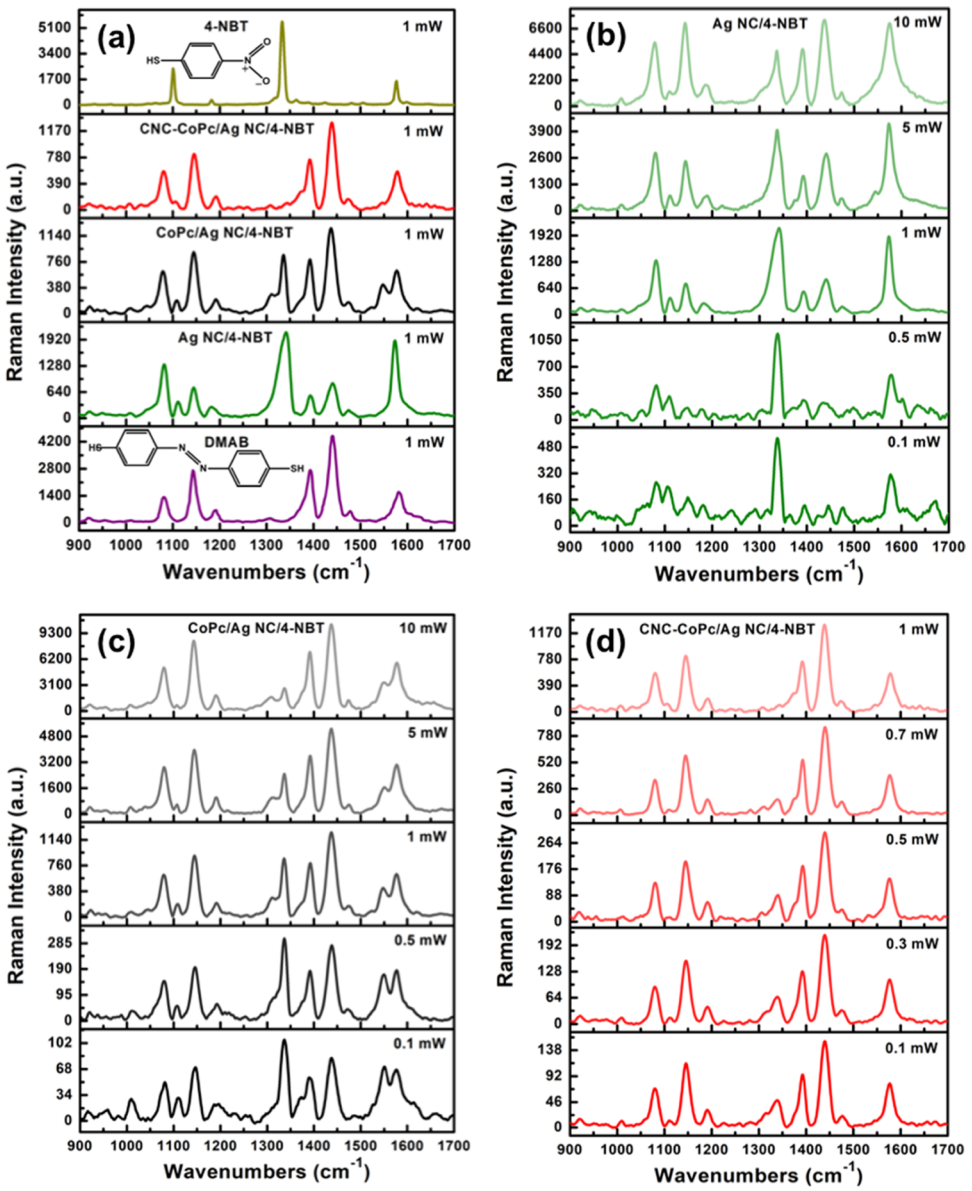

Figure 5. Surface catalytic conversion of 4-nitrobenzenethiol (4-NBT) to *p,p′*-dimercaptoazobenzene (DMAB) monitored by Raman spectroscopy. (a) Performance comparison for Ag nanoparticles and CoPc−Ag and CNC−CoPc−Ag systems at 1 mW laser power. Laser power-dependent spectral evolution of the reactant (4-NBT) and product (DMAB) for different systems: (b) Ag nanoparticles, (c) CoPc−Ag, and (d) CNC−CoPc−Ag. Raman spectra were accumulated for 5 × 15 s exposure time in air at room temperature (excitation wavelength 532 nm).

based electron transfer [Co(II)/Co(I)][70,71] appeared almost flattened out at around 0.3 V (vs Ag/AgCl). In the case for the CNC−CoPc conjugate, the ligand-based peak shifted to −0.7 V, while the metal-based peak remained almost unchanged. This is expected since, in the conjugate, the CNCs are covalently attached to the ring.

2.2. Photocatalytic Activities. *2.2.1. Surface Photocatalytic Transformation of 4-NBT to DMAB.* The photoreduction of 4-NBT to DMAB requires large kinetic energy to overcome the potential barrier and involves four electrons. The chemical structures of 4-NBT and DMAB are shown in Figure 5a (top and bottom insets, respectively). This photoreduction has been observed on plasmonic metal surfaces such as Au, Ag, and Cu.[73] When a plasmonic system comes in proximity to a semiconductor, it constitutes a hybrid that can act as an exciton−plasmon-coupled system or plexcitonic system.[27] There are a few reports in the current literature on hybrid systems, such as MoS_2−Ag,[74] TiO_2−Ag,[75] graphene oxide (GO)−Ag,[76] and nitrogen-doped graphene−Ag[77] systems, that exploited the synergistic exciton−plasmon codriven photocatalytic efficacy. Here, we have explored the surface photocatalytic activities of the plasmonic system bare Ag nanoparticles and the exciton−plasmon-coupled CoPc−Ag and CNC−CoPc−Ag systems. As mentioned in the Methodology section (Supporting Information), lab-grown Ag nanoparticles were drop-cast onto CoPc and CNC−CoPc substrates followed by thermal annealing prior to the photocatalytic test experiments. Figure S8a,b (Supporting Information) shows field-emission scanning electron microscopy (FESEM) images of a submonolayer of Ag nanoparticles on bare CoPc and CNC−CoPc substrates, respectively. Such dense arrangements of plasmonic Ag nanoparticles on semiconducting substrates are expected to enhance the local electromagnetic field under light illumination. These Ag

https://doi.org/10.1021/acs.jpcc.2c03531
J. Phys. Chem. C XXXX, XXX, XXX−XXX

nanoparticles have cubical geometries with curved corners (Figure S8e, Supporting Information). HRTEM images (Figure S8c,d, Supporting Information) show the fine structural features of these nanocubes. The obtained lattice spacing (*d*-spacing) for Ag nanocubes is 0.20 nm (Figure S8d, Supporting Information). This observation is consistent with the dominant lattice plane (111) of the Ag nanocubes found in the X-ray diffractometry pattern (Figure S8g, Supporting Information), where all of the peaks were associated with face-centered cubic silver.[78] Elemental analysis results collected in STEM mode are presented in Figure S8e,f,h (Supporting Information). These lab-grown Ag nanocubes have a negligible amount of oxygen, which indicates a desirable compositional attribute for plasmonic applications, either standalone or in a heterojunction with a semiconductor.

Ag nanoparticle drop-cast CoPc and CNC−CoPc samples were tested in the surface photocatalytic transformation of 4-NBT to DMAB through SERS (surface-enhanced Raman spectroscopy) experiments. Figure 5a shows the Raman spectra of 4-NBT and DMAB (top and bottom panels, respectively). The 4-NBT Raman peaks at 1101, 1332, and 1576 cm^{-1} have been assigned to a S−C stretching vibration, a NO_2 vibration, and a C═C stretching vibration of the benzyl rings, respectively, while DMAB Raman peaks at 1142 cm^{-1} originate from a C═N stretching vibration and peaks at 1392 and 1439 cm^{-1} are attributed to N═N stretching vibrations (ag_{16} and ag_{17} vibrational modes, respectively).[73,79−81] To study the comparative surface photocatalytic performances of pristine Ag, CoPc−Ag, and CNC−CoPc−Ag systems, we deposited an ultradilute 4-NBT solution on a submonolayer of Ag on bare glass, CoPc, and the CNC−CoPc substrates. We have conducted performance tests for surface photoreduction by varying the laser power from 0.1 to 10 mW. Figure 5b−d shows the gradual decrease of the main 4-NBT peak (1332 cm^{-1}) and a simultaneous gradual increase of the DMAB peaks for pristine Ag, CoPc−Ag, and CNC−CoPc−Ag systems, respectively, with a gradual laser power increase. These plots also indicate that the exciton−plasmon-coupled systems (CoPc and CNC−CoPc) are more efficient in this photocatalytic reaction than plasmonic Ag nanoparticles. Between the two former systems, CNC−CoPc is more efficient in photoreducing 4-NBT to DMAB. While it required a small laser of only 1 mW to completely convert the reactant to the product for the CNC−CoPc−Ag system (Figure 5b), a weak 4-NBT peak remains in the spectrum of CoPc−Ag at high laser power (10 mW) (Figure 5c). Relative to these exciton−plasmon-coupled systems, the bare plasmonic system Ag demonstrated the weakest activity in this photocatalysis. A dominant 4-NBT peak was detected at laser powers as high as 10 mW (Figure 5d). Figure 5a shows the comparative photoreduction efficiency of these three systems, which manifests in the following order: CNC−CoPc−Ag > CoPc−Ag > Ag. It is worth noting that a Raman peak at 1532 cm^{-1} (Figure S4a, Supporting Information) which originates due to out-of-phase stretching of C-N-C bridges resulting from a symmetric motion of four isoindole groups, was observed in this experiment for CoPc−Ag samples (Figure 5c). This peak was absent in CNC−CoPc−Ag (Figure 5d), probably due to a small loading of CoPc in the conjugate. This peak shifted to a higher wavenumber, 1547 cm^{-1}, probably as a result of the interaction of CoPc with Ag nanoparticles.

Plasmons are collective oscillations of conduction electrons, analogous to quantum harmonic oscillators composed of alternating regions of high and low electron densities.[82] In the case of pure plasmonic Ag nanoparticles, surface plasmon decay by nonradiative Landau damping, generated hot electrons in plasmonic metals are injected into 4-NBT with high kinetic energy, and are responsible for performing the photoreduction reaction.[73,76] The other possible route of photoreduction by these Ag nanoparticles would involve direct chemical interface damping, where 4-NBT molecules are in direct physical contact with Ag nanoparticles and Landau damping of plasmon-generated hot electrons is not necessary.[83] On the other hand, in exciton−plasmon-coupled systems, a simultaneous increase in the plasmon to electron conversion efficiency and the hot electron lifetime has been reported.[74,75,84] These dual effects resulted in superior photocatalytic performance in the CNC−CoPc−Ag and CoPc−Ag plexcitonic systems compared to that of standalone plasmonic Ag. Exciton−plasmon coupling can take place by different routes, such as plasmon-induced far-field scattering or trapping of light in a semiconductor, hot electron and hot hole generation and injection into a semiconductor following Landau damping of plasmons, and plasmon-induced resonant energy transfer, which occurs due to dipole−dipole coupling in the near-field.[85−87] The remarkable improvement of surface photoreduction capability of CoPc upon covalent attachment with CNC can be rationalized from a few observations. Figure 4a shows the enhanced optical absorption in the conjugate compared to bare CoPc at the Raman excitation wavelength (532 nm), desirable for photocatalysis. A suppressed radiative recombination in the CNC−CoPc conjugate was observed from steady-state photoluminescence (Figures 4b and S5). Because of the above-mentioned phenomena, KPFM demonstrated a much larger shift of the surface potential for CNC−CoPc compared to that for bare CoPc (Figure 4), which indicated an enhancement of charge carriers in the conjugate system. A noteworthy result that emerged from KPFM measurements is the unusual direction of charge transfer. A more fundamental and supportive explanation for this enhanced charge carriers that resulted in improved photoreduction performance of the conjugate is presented with the results obtained from density functional theory (DFT) calculations later in this report.

2.2.2. Photocatalytic Degradation of Rhodamine B. In addition to the Raman surface photocatalytic performance of the plasmon-coupled CNC−CoPc described above, the as-synthesized conjugate without any attached plasmonic nanoparticle has been tested for RhB dye degradation. There are a few reports in the literature that attempted to explore this aspect of CoPc. While phthalocyanines such as CoPc are often used to sensitize the other active photocatalyst to enhance RhB degradation,[88] standalone CoPc has not been reported to perform this reaction under visible light without any added oxidant. H_2O_2 has been added to allow an efficient oxidation reaction using CoPc attached to cellulose fiber.[22,23,89] Addition of an oxidant has also been found effective in benzyl alcohol degradation by CoPc.[90] Biopolymer chitosan has been attached with CoPc to degrade RhB under UV light.[91] Bare tetracarboxylated CoPc did not adsorb nor did it show any activity toward degradation of RhB, according to the reported work by Marinescu et al.[92] In this work, we report that the coupled octacarboxylated CoPc and CNC system can at least perform this reaction to some degree, without any added oxidant under visible light.

https://doi.org/10.1021/acs.jpcc.2c03531
J. Phys. Chem. C XXXX, XXX, XXX−XXX

Figures S9 and S10 (Supporting Information) show an RhB degradation performance test for bare octacarboxylated CoPc and CNC−CoPc conjugated systems under AM1.5G one sun simulated sunlight, where 10 mg of photocatalysts has been used. Bare CoPc adsorbed RhB in the initial 30 min dark cycle period and did not show any photocatalytic activity at all since the remaining ∼10% dye (after dwelling time of 60 min in the dark) did not undergo any concentration decrease even after 80 min illumination, evidenced by the flat line in the concentration vs time plot (Figure S9a). This result shows that octacarboxylated CoPc can be used for high RhB adsorption applications. Even the addition of only 5 mg of bare CoPc to the RhB solution resulted in the disappearance of the majority of the RhB in the first 30 min of the dark cycle (Figure S11, Supporting Information). On the other hand, the CNC−CoPc conjugate also showed some adsorption behavior (Figures S9 and S10, Supporting Information), but additionally, it showed some photocatalytic performance, evidenced by the decreasing concentration of the dye with respect to illumination time. Notice that the slow decrease of dye concentration when the CNC−CoPc conjugate is added to the solution can be a result of slow adsorption in this system and may not be a consequence of photocatalytic degradation. To test the scenario, we have added 10 mg of CNC−CoPc conjugate in two different RhB solutions, followed by keeping one of them in the continuous dark and the other one in illumination conditions (Figures S9b and S10, Supporting Information). In the conjugate, the weight percentage of CoPc is only ∼20%; thus, this 10 mg of material contains only 2 mg of CoPc. From these figures, it is clearly visible that even though RhB keeps adsorbing on CNC−CoPc at a very slow rate, it goes through photocatalytic degradation, as the illumination curve has a steeper slope compared to the dark slope (Figure S9b). Thus, CoPc when covalently attached to the CNC surface does demonstrate its ability to degrade RhB in light. According to one previous work, tetracarboxylated CoPc does not adsorb nor degrade RhB.[92] The RhB dye can be degraded once molecular structure deformation occurs. This can be realized by two major routes, namely, chromophore cleavage (RhB ring attack) or cycloreversion and *N*-deethylation[93,94] (Figure S9b, inset). The first route involves photogenerated electrons in the conduction band of a semiconductor for the generation of strong oxidative reactants, such as superoxide radicals ($O^{\bullet -}$), hydroperoxyl radicals ($HO_2^{\bullet}$), and hydroxyl radicals ($OH^{\bullet}$). The photoelectrons need to possess high reduction potential for the generation of $O^{\bullet -}$ from molecular oxygen. $HO_2^{\bullet}$ and $OH^{\bullet}$ can be generated from these superoxide radicals as a result of a reaction with protons (H^+) and e^-. The oxidative reactants, $O^{\bullet -}$, $HO_2^{\bullet}$, and $OH^{\bullet}$ have the ability to degrade RhB by a chromophore cleavage mechanism.[94] The required H^+ for the generation of $HO_2^{\bullet}$ and $OH^{\bullet}$ from $O^{\bullet -}$ can be achieved from water oxidation.[95] The hydroxyl radical ($OH^{\bullet}$) can be generated from another route, that is, from H_2O by photogenerated holes (h^+) in the valence band of a semiconductor, which requires a very high oxidation potential.[95] In the second route, namely, *N*-deethylation, a dye cation radical is formed through oxidation of the dye in the presence of a strong electron acceptor. The photogenerated holes in the semiconductor valence band react with such an RhB cation radical by eliminating one alkyl group in this *N*-deethylation mechanism.[93,96] To get more insight into the RhB degradation mechanisms, we performed a scavenger test. Figures S9a and S10d,e (Supporting Information) show the scavenger test results with electron and hole scavengers $AgNO_3$ and ethylenediaminetetraacetic acid (EDTA), respectively. When EDTA is added, the hole is removed, which can diminish the latter route but simultaneously enhance the former pathway. A suppressed activity confirms that electrons do not play any role here. On the other hand, when $AgNO_3$ is added, the degradation pathway shifts predominantly toward the *N*-deethylation route, as only the hole is the active carrier. In this case, we see a gradual peak shift toward a lower wavelength during illumination conditions (Figure S10d, Supporting Information), consistent with an earlier report that showed the correlation between reaction pathways and time evolution of the peak position, where such a hypsochromic shift has been associated with the *N*-deethylation mechanism.[97] The RhB degradation results discussed above have been summarized in Table S1 (Supporting Information). Figure S12 (Supporting Information) shows the steady-state photoluminescence spectra of bare RhB, bare CoPc immersed in the aqueous RhB solution, and the CNC−CoPc conjugate immersed in the aqueous RhB solution. As expected, the CoPc-containing RhB solution did not show any RhB emission peak due to the dye adsorption property of bare octacarboxylated CoPc, as discussed earlier. On the other hand, the CNC−CoPc-containing RhB solution did show the RhB emission peak.

2.3. Theoretical Modeling and Computational Results. The stability of the CoPc-conjugated CNC has been theoretically investigated by employing a detailed study of the covalent attachment using periodic self-consistent DFT calculations. For physiosorbed or chemisorbed systems, generally, the binding energy calculation of the adsorbate to the substrate surface is a standard quantitative approach to determine the stability of coupled systems. This binding energy can be calculated by subtracting the total energy of the composite system from the sum of individual total energies of the adsorbate and the substrate, albeit considering their respective geometry-optimized structures.[98] Unfortunately, in the present system, this approach is not applicable since, for the requirement of ester bond formation, octacarboxylated CoPc has to lose OH from a −COOH group and CNC has to lose H from a surface hydroxyl group (−OH) in the CNC−CoPc conjugate system. Therefore, the conjugated system will have a smaller number of atoms than the total number of atoms of the individual systems. This scenario prompted us to study the binding between CoPc and CNC in a rather more qualitative fashion. We have analyzed the bonding between CNC and CoPc by the projected density of states (PDOS), which can be obtained by projecting the total wave function onto the orthogonalized atomic wave functions, and by electron density difference plots. The binding strength between CNC and CoPc has been investigated by the observation of PDOS overlap between the bonding atoms, which are oxygen atoms from the CNC surface hydroxyl group and carbon atoms from the carboxyl group of CoPc. Overlap analysis of PDOS can serve as an indicator of the strength of covalent attachment,[2] an alternate to some other methods such as density overlap region indicator analysis.[99] Figure S14 (Supporting Information) shows the PDOS of the oxygen (CNC) and carbon (CoPc) atoms. The phthalocyanine rings are oriented vertically (Figure S14a,b) on the hydrophilic ($1\bar{1}0$) and hydrophobic (200) planes,[100] while Figure S14c,d shows the horizontal configuration, respectively. The electronic states in both the occupied and unoccupied regions are

https://doi.org/10.1021/acs.jpcc.2c03531
J. Phys. Chem. C XXXX, XXX, XXX−XXX

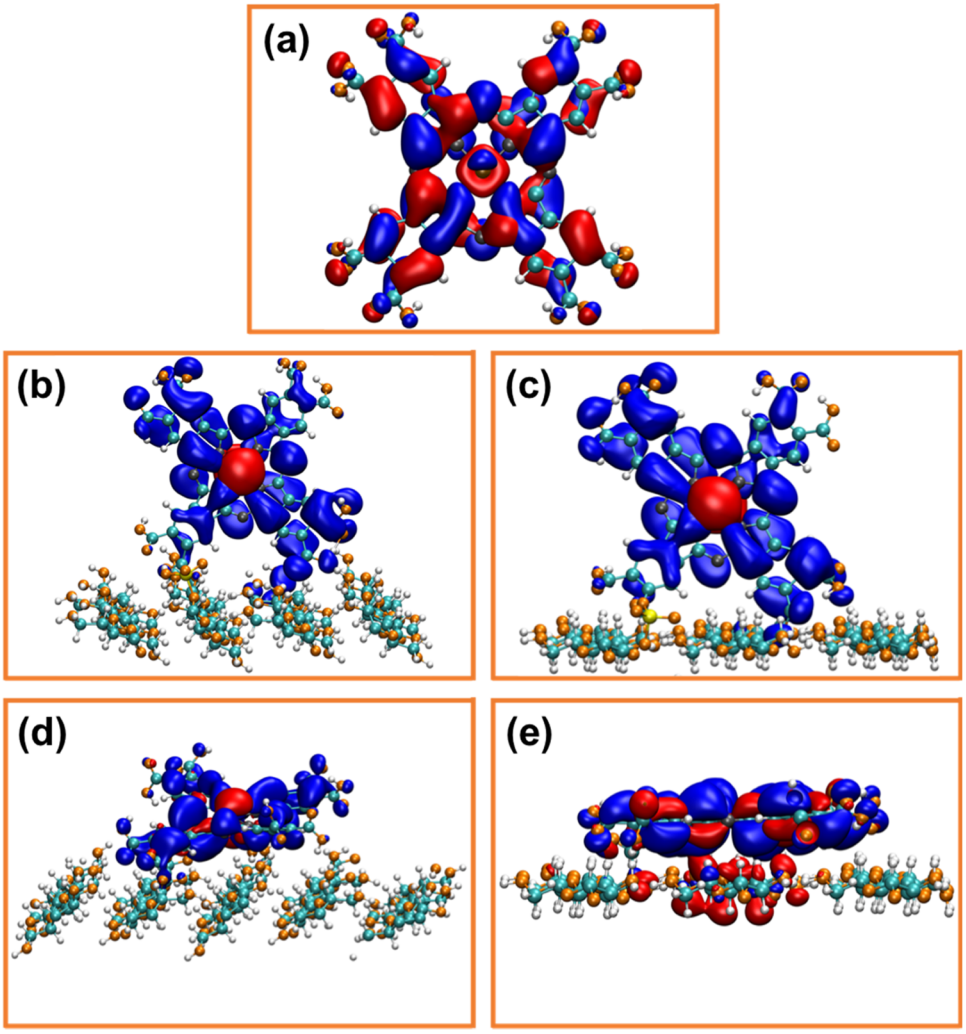

Figure 6. Spatial distributions of molecular orbitals for (a) pristine CoPc and (b)−(e) CNC−CoPc conjugated systems. Metallophthalocyanine rings oriented vertically to the CNC surface for (b) hydrophilic plane ($1\bar{1}0$) and (c) hydrophobic plane (200). Metallophthalocyanine rings oriented horizontally to the CNC surface for (d) hydrophilic plane ($1\bar{1}0$) and (e) hydrophobic plane (200). HOMO and LUMO orbitals are represented by red and blue surfaces, respectively. The colors for C, O, H, S, N, and Co atoms are cyan, orange, white, yellow, gray, and brown, respectively.

overlapped in terms of energy of states, while intensity distributions are dissimilar. Oxygen atoms have more states in occupied regions than carbon atoms, while PDOS intensities of carbon atoms are much higher than those of oxygen atoms in the unoccupied region. Figure S15 (Supporting Information) shows the electron density difference isosurfaces of all of the conjugated systems shown in Figure S14. The pink and tan surfaces represent negative and positive isosurfaces corresponding to charge depletion and accumulation regions, respectively. Thus, the electron density difference results are in complete harmony with the PDOS intensity differences between O and C atoms in the occupied and unoccupied regions near the Fermi level.

Spatial distributions of the highest occupied molecular orbital (HOMO) and the lowest unoccupied molecular orbital (LUMO) of pristine CoPc and CNC−CoPc conjugated systems calculated by DFT are shown in Figure 6. Molecular orbitals (both HOMO and LUMO) of bare CoPc (Figure 6a) are closely spaced and delocalized over the entire molecule including the Co atom. An earlier study based on a quasirelativistic approach that used the Vosko−Wilk−Nusair (VWN) local spin-density potential plus Becke's gradient correction for exchange and Perdew's gradient correction for correlation also reported that HOMO localization occurs on metal atoms for Co, Fe, and Cu phthalocyanine, unlike Zn and Ni, where HOMO localization occurs only on the phthalocyanine ring.[101] We considered two geometries for covalent conjugation of CoPc on the CNC surface. In the case when metallophthalocyanine rings orient vertically to the CNC surface for the hydrophilic ($1\bar{1}0$) and hydrophobic (200) planes, the HOMO is entirely localized on the central Co atom (Figure 6b,c). This spatial separation of molecular orbitals is relatively less in other configurations, when the metallophthalocyanine rings orient horizontally to the CNC surface, for the ($1\bar{1}0$) and (200) planes (Figure 6d,e). Therefore, our DFT calculations revealed an overall pronounced spatial separation of HOMO and LUMO, which facilitates exciton dissociation and prolongs exciton lifetime.[102] The previously discussed large surface potential shift in the conjugate, as a consequence of the increased photoinduced charge accumulation, also aligns with these theoretical findings. This spatial separation of molecular orbitals is expected to promote a

https://doi.org/10.1021/acs.jpcc.2c03531
J. Phys. Chem. C XXXX, XXX, XXX−XXX

photoinduced intramolecular charge-transfer transition.[103] Unlike closed shell structures such as ZnPc or MgPc, metallophthalocyanines with open shells, such as CoPc, promote intramolecular charge-transfer transitions.[61] Thus, our earlier discussion on the enhanced absorption in the spectral range of 400−600 nm in CNC−CoPc compared to that in bare CoPc, mediated by an intramolecular charge-transfer transition, is in complete harmony with the DFT-computed molecular orbital localization results. On the other hand, for CoPc, intramolecular relaxation is a much faster process than energy transfer to the surface plasmons generated by Ag.[104] The enhanced spatial separation of molecular orbitals in the conjugate is expected to suppress the faster intramolecular relaxation (since it facilitates exciton dissociation) and strengthen the interaction with surface plasmons (exciton−plasmon coupling) through different possible mechanisms in the plexcitonic systems mentioned earlier.

Figure S16 (Supporting Information) shows the total density of states (DOS) and the projected density of states (PDOS) of the Co atom (d-orbital only) for the pristine CoPc and the CNC−CoPc conjugated systems. Three important observations are found from these plots. First, in the conjugates, more states appear corresponding to more energy levels, both in the occupied and unoccupied regions near the Fermi level. Second, the HOMO−LUMO gap shrinks in the conjugates in comparison to that in pristine CoPc. The HOMO−LUMO gaps for the systems are 1.52, 1.26, 1.30, 1.46, and 1.41 eV for bare CoPc, CoPc oriented vertically to the CNC hydrophilic plane ($1\bar{1}0$) and hydrophobic plane (200), and CoPc oriented horizontally to the CNC hydrophilic plane ($1\bar{1}0$) and hydrophobic plane (200), respectively. Note that, in all configurations of the conjugate, the HOMO−LUMO gap is reduced specifically in the vertical geometries. Third, in CNC−CoPc conjugates, the d-orbital energy states have less intensity near the HOMO in the occupied region compared to bare CoPc (Figure S16, Supporting Information). Open shell metallophthalocyanines, such as CoPc, are known for promoting faster excited-state dynamics compared to metal-free phthalocyanine due to the presence of a metal atom.[105] The above observation implies less contribution from 3d orbitals to the occupied orbitals in the vicinity of the HOMO. CoPc are known to have several 3d-like orbitals near the HOMO,[101] so there will be less coupling between Co atom 3d-electrons and π-orbitals of the phthalocyanine framework, which implies that faster excited-state relaxation is suppressed;[105] in other words, the exciton lifetime is increased in the conjugated systems compared to that in standalone CoPc. Coupling between π-orbitals and d-electrons creates additional energy relaxation channels.[105,106] Thus, enhanced charge separation is expected in the conjugates through prolonged excited-state lifetimes. In summary, theoretical calculations revealed two major phenomena in CNC−CoPc conjugates compared to bare CoPc, (a) enhanced HOMO−LUMO spatial separation, which facilitates exciton dissociation, and (b) the reduced intensity of 3d-like states in the vicinity of HOMO, which results in longer exciton lifetimes. Both these effects are conducive to stronger exciton−plasmon coupling and can potentially accelerate photocatalytic reactions, as evidenced by Raman surface photocatalytic transformation of 4-NBT to DMAB and RhB photodegradation test results.

3. CONCLUSIONS

We have successfully synthesized octacarboxylated cobalt phthalocyanine conjugated cellulose nanocrystals by ester bond formation between them. Several routine and advanced characterization techniques were used to investigate the properties of the covalently bonded system. Experimental results from XPS, solid-state NMR, XRD, HRTEM, STEM-EDX elemental mapping, Raman spectroscopy, FTIR spectroscopy, UV−vis absorption, and steady-state PL spectroscopy confirm the successful conjugation and indicate reduced aggregation of CoPc on the surface of CNC. The covalent attachment of CoPc on the CNC surface was analyzed by DFT calculations through the projected density of states onto the bond-forming atoms and electron density difference plots, which indicated a stable conjugated system. KPFM results indicated an enhanced charge carrier generation and long-lived charge separation upon illumination in the CNC−CoPc conjugate compared to standalone CoPc with photogenerated holes remaining on CoPc and photogenerated electrons transferred to CNCs. The synthesized pristine CoPc and the conjugate were tested as catalysts for the photocatalytic transformation of 4-NBT to DMAB and also for RhB photodegradation. In both experiments, the CNC−CoPc system demonstrated superior photocatalytic activities compared to pristine CoPc. Upon conjugation to the CNC surface, CoPc molecules undergo a change in aggregation state, which results in an increased surface area. Molecular orbital and density of states results from DFT calculations implied enhanced exciton dissociation and prolonged exciton lifetime in the conjugate; both are expected to increase the exciton−plasmon coupling strength that resulted in improved photocatalytic performance for the 4-NBT to DMAB transformation. Such results also align well with the RhB degradation data and explain the superior photocatalytic activity observed in spite of the large exciton binding energy of CoPc. This work demonstrates the potential for cellulose nanocrystals to function not merely as a support template to increase the effective area but also as an integral element to tune the electronic properties of the active material in a desirable fashion for functional optoelectronic device applications.

■ ASSOCIATED CONTENT

Supporting Information

The Supporting Information is available free of charge at https://pubs.acs.org/doi/10.1021/acs.jpcc.2c03531.

Experimental and modeling methods, schematic illustration of the CNC−CoPc conjugation protocol, additional XPS spectra, ^{13}C solid-state NMR spectra, Raman and FTIR spectra, excitation-dependent Soret band emission spectra, surface topographic AFM (a) height and (b) phase images of CNC−CoPc on FTO, additional photocatalytic activity data related to rhodamine B degradation, CNC segment considered for large-scale molecular dynamics simulations, and additional results from DFT computations (PDF)

■ AUTHOR INFORMATION

Corresponding Author

Karthik Shankar − *Department of Electrical and Computer Engineering, University of Alberta, Edmonton, AB T6G 1H9, Canada;* orcid.org/0000-0001-7347-3333;
Email: kmalam@ualberta.ca, kshankar@ualberta.ca

https://doi.org/10.1021/acs.jpcc.2c03531
J. Phys. Chem. C XXXX, XXX, XXX−XXX

Authors

Kazi M. Alam − *Department of Electrical and Computer Engineering, University of Alberta, Edmonton, AB T6G 1H9, Canada; Nanotechnology Research Centre, National Research Council Canada, Edmonton, AB T6G 2M9, Canada;* orcid.org/0000-0001-5075-5928

Pawan Kumar − *Department of Electrical and Computer Engineering, University of Alberta, Edmonton, AB T6G 1H9, Canada*

Narendra Chaulagain − *Department of Electrical and Computer Engineering, University of Alberta, Edmonton, AB T6G 1H9, Canada*

Sheng Zeng − *Department of Electrical and Computer Engineering, University of Alberta, Edmonton, AB T6G 1H9, Canada*

Ankur Goswami − *Department of Electrical and Computer Engineering, University of Alberta, Edmonton, AB T6G 1H9, Canada; Department of Materials Science and Engineering, Indian Institute of Technology Delhi, New Delhi 11016, India;* orcid.org/0000-0003-0639-6758

John Garcia − *Department of Electrical and Computer Engineering, University of Alberta, Edmonton, AB T6G 1H9, Canada;* orcid.org/0000-0002-5964-5781

Ehsan Vahidzadeh − *Department of Electrical and Computer Engineering, University of Alberta, Edmonton, AB T6G 1H9, Canada*

Manish L. Bhaiyya − *MEMS, Microfluidics and Nanoelectronics (MMNE) Lab, Department of Electrical and Electronics Engineering, Birla Institute of Technology and Science, Pilani, Hyderabad 500078, India*

Guy M. Bernard − *Department of Chemistry, University of Alberta, Edmonton, AB T6G 2G2, Canada;* orcid.org/0000-0003-1507-6705

Sanket Goel − *MEMS, Microfluidics and Nanoelectronics (MMNE) Lab, Department of Electrical and Electronics Engineering, Birla Institute of Technology and Science, Pilani, Hyderabad 500078, India;* orcid.org/0000-0002-9739-4178

Vladimir K. Michaelis − *Department of Chemistry, University of Alberta, Edmonton, AB T6G 2G2, Canada;* orcid.org/0000-0002-6708-7660

Alexander E. Kobryn − *Nanotechnology Research Centre, National Research Council Canada, Edmonton, AB T6G 2M9, Canada*

Sergey Gusarov − *Nanotechnology Research Centre, National Research Council Canada, Edmonton, AB T6G 2M9, Canada;* orcid.org/0000-0003-2033-705X

Complete contact information is available at: https://pubs.acs.org/10.1021/acs.jpcc.2c03531

Author Contributions

K.M.A. conceptualized and led the research project and contributed to material synthesis, experimental data collection and data interpretation, theoretical calculations, and manuscript writing. P.K. conceptualized the synthesis protocol and contributed to material synthesis and XPS and NMR data interpretation. N.C. prepared samples for RhB dye degradation and contributed to data collection and organization. S.Z. contributed to Raman data acquisition and organization. A.G. prepared samples for KPFM measurements and collected data. J.G. helped in dye degradation experiments. E.V. synthesized the silver nanocubes. M.B. contributed to experimental data collection for cyclic voltammetry. G.M.B. collected NMR data and contributed to data interpretation and editing. S.G. supervised M.B. V.K.M. supervised NMR data acquisition, interpretation, and editing. A.E.K. and S.G. supervised and contributed to theoretical (molecular dynamics and DFT) modeling and computations. K.S. supervised the research project, contributed to experimental data interpretation, and edited the whole manuscript.

Notes

The authors declare no competing financial interest.

■ ACKNOWLEDGMENTS

The authors acknowledge direct and indirect funding support from the National Research Council Canada (NRC), NSERC, Alberta Innovates, Future Energy Systems, and FPInnovations. The cellulose nanocrystals were provided by InnoTech Alberta. University of Alberta NanoFAB staff member Anqiang He is acknowledged for collecting HRTEM/EDX data for the CNC−CoPc sample. National Research Council staff member Kai Cui is acknowledged for collecting HRTEM/EDX data for the Ag nanoparticles. The authors thank Shiraz Merali (Chemical Technologist, Chemical and Materials Engineering Department, University of Alberta) for collecting AAS data.

■ REFERENCES

(1) Marschall, R. Semiconductor Composites: Strategies for Enhancing Charge Carrier Separation to Improve Photocatalytic Activity. *Adv. Funct. Mater.* **2014**, *24*, 2421−2440.

(2) Wang, H.; Sun, Y.; He, W.; Zhou, Y.; Lee, S. C.; Dong, F. Visible Light Induced Electron Transfer from a Semiconductor to an Insulator Enables Efficient Photocatalytic Activity on Insulator-Based Heterojunctions. *Nanoscale* **2018**, *10*, 15513−15520.

(3) Grodkowski, J.; Dhanasekaran, T.; Neta, P.; Hambright, P.; Brunschwig, B. S.; Shinozaki, K.; Fujita, E. Reduction of Cobalt and Iron Phthalocyanines and the Role of the Reduced Species in Catalyzed Photoreduction of CO_2. *J. Phys. Chem. A* **2000**, *104*, 11332−11339.

(4) Morlanés, N.; Takanabe, K.; Rodionov, V. Simultaneous Reduction of CO_2 and Splitting of H_2O by a Single Immobilized Cobalt Phthalocyanine Electrocatalyst. *ACS Catal.* **2016**, *6*, 3092−3095.

(5) Zhang, X.; Wu, Z.; Zhang, X.; Li, L.; Li, Y.; Xu, H.; Li, X.; Yu, X.; Zhang, Z.; Liang, Y.; Wang, H. Highly Selective and Active CO_2 Reduction Electrocatalysts Based on Cobalt Phthalocyanine/Carbon Nanotube Hybrid Structures. *Nat. Commun.* **2017**, *8*, No. 14675.

(6) Reisner, S. R. E.; Reisner, E. Visible-Light-Driven CO_2 Reduction by Mesoporous Carbon Nitride Modified with Polymeric Cobalt Phthalocyanine. *Angew. Chem., Int. Ed.* **2019**, *58*, 12180−12184.

(7) Ji, X.; Zou, T.; Gong, H.; Wu, Q.; Qiao, Z.; Wu, W.; Wang, H. Cobalt Phthalocyanine Nanowires: Growth, Crystal Structure, and Optical Properties. *Cryst. Res. Technol.* **2016**, *51*, 154−159.

(8) Martínez-Díaz, M. V.; de la Torre, G.; Torres, T. Lighting Porphyrins and Phthalocyanines for Molecular Photovoltaics. *Chem. Commun.* **2010**, *46*, 7090−7108.

(9) Kisslinger, R.; Hua, W.; Shankar, K. Bulk Heterojunction Solar Cells Based on Blends of Conjugated Polymers with II−VI and IV−VI Inorganic Semiconductor Quantum Dots. *Polymers* **2017**, *9*, No. 35.

(10) Luppi, B. T.; Majak, D.; Gupta, M.; Rivard, E.; Shankar, K. Triplet Excitons: Improving Exciton Diffusion Length for Enhanced Organic Photovoltaics. *J. Mater. Chem. A* **2019**, *7*, 2445−2463.

(11) Klemm, D.; Heublein, B.; Fink, H. P.; Bohn, A. Cellulose: Fascinating Biopolymer and Sustainable Raw Material. *Angew. Chem., Int. Ed.* **2005**, *44*, 3358−93.

https://doi.org/10.1021/acs.jpcc.2c03531
J. Phys. Chem. C XXXX, XXX, XXX−XXX

(12) Habibi, Y. L.; Lucian, A.; Rojas, O. J. Cellulose Nanocrystals: Chemistry, Self-Assembly, and Applications. *Chem. Rev.* **2010**, *110*, 3479−3500.
(13) Xie, S.; Zhang, X.; Walcott, M. P.; Lin, H. Applications of Cellulose Nanocrystals:a Review. *Eng. Sci.* **2018**, *2*, 4−16.
(14) Cirtiu, C. M.; Dunlop-Brière, A. F.; Moores, A. Cellulose Nanocrystallites as an Efficient Support for Nanoparticles of Palladium: Application for Catalytic Hydrogenation and Heck Coupling under Mild Conditions. *Green Chem.* **2011**, *13*, 288−291.
(15) Awan, F.; Islam, M. S.; Ma, Y.; Yang, C.; Shi, Z.; Berry, R. M.; Tam, K. C. Cellulose Nanocrystal-Zno Nanohybrids for Controlling Photocatalytic Activity and UV Protection in Cosmetic Formulation. *ACS Omega* **2018**, *3*, 12403−12411.
(16) Risteen, B.; McBride, M.; Gonzalez, M.; Khau, B.; Zhang, G.; Reichmanis, E. Functionalized Cellulose Nanocrystal-Mediated Conjugated Polymer Aggregation. *ACS Appl. Mater. Interfaces* **2019**, *11*, 25338−25350.
(17) Alam, K. M.; Kar, P.; Thakur, U. K.; Kisslinger, R.; Mahdi, N.; Mohammadpour, A.; Baheti, P. A.; Kumar, P.; Shankar, K. Remarkable Self-Organization and Unusual Conductivity Behavior in Cellulose Nanocrystal-PEDOT: PSS Nanocomposites. *J. Mater. Sci.: Mater. Electron.* **2019**, *30*, 1390−1399.
(18) Silva, A. C. D.; Moura Filho, F.; Alves, M. R. A.; de Menezes, A. J.; Silva, M. C. Hybrid Organic Semiconductors from P3HT and Cellulose Nanocrystals Modified with 3-Thiopheneacetic Acid. *Synth. Met.* **2021**, *278*, No. 116804.
(19) Unuma, T.; Kobayashi, O.; Kotaka, S.; Koppolu, R.; Toivakka, M.; Saarinen, J. J. Terahertz Complex Conductivity of Cellulose Nanocrystal Based Composite Films Controlled with PEDOT:PSS Blending Ratio. *Cellulose* **2020**, *27*, 10019−10027.
(20) Chauhan, P.; Yan, N. Nanocrystalline Cellulose Grafted Phthalocyanine: A Heterogeneous Catalyst for Selective Aerobic Oxidation of Alcohols and Alkyl Arenes at Room Temperature in a Green Solvent. *RSC Adv.* **2015**, *5*, 37517−37520.
(21) Shaabani, A.; Keshipour, S.; Hamidzad, M.; Shaabani, S. Cobalt(Ii) Phthalocyanine Covalently Anchored to Cellulose as a Recoverable and Efficient Catalyst for the Aerobic Oxidation of Alkyl Arenes and Alcohols. *J. Mol. Catal. A: Chem.* **2014**, *395*, 494−499.
(22) Chen, S.-L.; Huang, X.-J.; Xu, Z.-K. Functionalization of Cellulose Nanofiber Mats with Phthalocyanine for Decoloration of Reactive Dye Wastewater. *Cellulose* **2011**, *18*, 1295−1303.
(23) Chen, S.-L.; Huang, X.-J.; Xu, Z.-K. Effect of a Spacer on Phthalocyanine Functionalized Cellulose Nanofiber Mats for Decolorizing Reactive Dye Wastewater. *Cellulose* **2012**, *19*, 1351−1359.
(24) Alam, K. M.; Kumar, P.; Gusarov, S.; Kobryn, A. E.; Kalra, A. P.; Zeng, S.; Goswami, A.; Thundat, T.; Shankar, K. Synthesis and Characterization of Zinc Phthalocyanine-Cellulose Nanocrystal (CNC) Conjugates: Toward Highly Functional Cncs. *ACS Appl. Mater. Interfaces* **2020**, *12*, 43992−44006.
(25) Chaulagain, N.; Alam, K. M.; Kumar, P.; Kobryn, A. E.; Gusarov, S.; Shankar, K. Zinc Phthalocyanine Conjugated Cellulose Nanocrystals for Memory Device Applications. *Nanotechnology* **2021**, *33*, No. 055703.
(26) Achermann, M. Exciton−Plasmon Interactions in Metal−Semiconductor Nanostructures. *J. Phys. Chem. Lett.* **2010**, *1*, 2837−2843.
(27) Manuel, A. P.; Kirkey, A.; Mahdi, N.; Shankar, K. Plexcitonics—Fundamental Principles and Optoelectronic Applications. *J. Mater. Chem. C* **2019**, *7*, 1821−1853.
(28) Dong, X. M.; Revol, J.-F.; Gray, D. G. Effect of Microcrystallite Preparation Conditions on the Formation of Colloid Crystals of Cellulose. *Cellulose* **1998**, *5*, 19−32.
(29) Burkitt, R.; Whiffen, T. R.; Yu, E. H. Iron Phthalocyanine and MnO_x Composite Catalysts for Microbial Fuel Cell Applications. *Appl. Catal., B* **2016**, *181*, 279−288.
(30) Kim, J. H.; Sa, Y. J.; Jeong, H. Y.; Joo, S. H. Roles of Fe-N_x and Fe-Fe_3C@C Species in Fe-N/C Electrocatalysts for Oxygen Reduction Reaction. *ACS Appl. Mater. Interfaces* **2017**, *9*, 9567−9575.
(31) Zhang, Y.; Learmonth, T.; Wang, S.; Matsuura, A. Y.; Downes, J.; Plucinski, L.; Bernardis, S.; O'Donnell, C.; Smith, K. E. Electronic Structure of the Organic Semiconductor Vanadyl Phthalocyanine (VO-Pc). *J. Mater. Chem.* **2007**, *17*, 1276−1283.
(32) Tao, C.-a.; Wang, J.; Qin, S.; Lv, Y.; Long, Y.; Zhu, H.; Jiang, Z. Fabrication of pH-Sensitive Graphene Oxide−Drug Supramolecular Hydrogels as Controlled Release Systems. *J. Mater. Chem.* **2012**, *22*, 24856−24861.
(33) Subramanian, P.; Schechter, A. Electrochemical Oxygen Reduction Activity of Cobalt-Nitrogen-Carbon Composite Catalyst Prepared by Single Precursor Pyrolysis under Autogenic Pressure. *J. Electrochem. Soc.* **2016**, *163*, F428−F436.
(34) Kumar, A.; Samanta, S.; Latha, S.; Debnath, A. K.; Singh, A.; Muthe, K. P.; Barshilia, H. C. Enhanced Cl_2 Sensitivity of Cobalt-Phthalocyanine Film by Utilizing a Porous Nanostructured Surface Fabricated on Glass. *RSC Adv.* **2017**, *7*, 4135−4143.
(35) Tran, T. N.; Paul, U.; Heredia-Guerrero, J. A.; Liakos, I.; Marras, S.; Scarpellini, A.; Ayadi, F.; Athanassiou, A.; Bayer, I. S. Transparent and Flexible Amorphous Cellulose-Acrylic Hybrids. *Chem. Eng. J.* **2016**, *287*, 196−204.
(36) Smith, M.; Scudiero, L.; Espinal, J.; McEwen, J.-S.; Garcia-Perez, M. Improving the Deconvolution and Interpretation of XPS Spectra from Chars by Ab Initio Calculations. *Carbon* **2016**, *110*, 155−171.
(37) Qiu, B.; Wang, Y.; Sun, D.; Wang, Q.; Zhang, X.; Weeks, B. L.; O'Connor, R.; Huang, X.; Wei, S.; Guo, Z. Cr(Vi) Removal by Magnetic Carbon Nanocomposites Derived from Cellulose at Different Carbonization Temperatures. *J. Mater. Chem. A* **2015**, *3*, 9817−9825.
(38) Schmid, M.; Kaftan, A.; Steinrück, H.-P.; Gottfried, J. M. The Electronic Structure of Cobalt(II) Phthalocyanine Adsorbed on Ag(111). *Surf. Sci.* **2012**, *606*, 945−949.
(39) Kunze, J. F. HHP Characterization of Cellulose and Cellulose Derivatives by High Resolution Solid State ^{13}C Nmr Spectroscopy. *Papier* **1999**, *53*, 753−764.
(40) Kazmi, M. Z. H.; Karmakar, A.; Michaelis, V. K.; Williams, F. J. Separation of Cellulose/Hemicellulose from Lignin in White Pine Sawdust Using Boron Trihalide Reagents. *Tetrahedron* **2019**, *75*, 1465−1470.
(41) Gil, A. M.; Neto, C. P. Solid-State NMR Studies of Wood and Other Lignocellulosic Materials. In *Annual Reports On NMR Spectroscopy*; Academic Press, 1999; Vol. *37*, pp 75−117.
(42) Takahashi, H.; Lee, D.; Dubois, L.; Bardet, M.; Hediger, S.; De Paëpe, G. Rapid Natural-Abundance 2D ^{13}C-^{13}C Correlation Spectroscopy Using Dynamic Nuclear Polarization Enhanced Solid-State Nmr and Matrix-Free Sample Preparation. *Angew. Chem., Int. Ed.* **2012**, *51*, 11766−11769.
(43) Yu, H.; Qin, Z.; Liang, B.; Liu, N.; Zhou, Z.; Chen, L. Facile Extraction of Thermally Stable Cellulose Nanocrystals with a High Yield of 93% through Hydrochloric Acid Hydrolysis under Hydrothermal Conditions. *J. Mater. Chem. A* **2013**, *1*, 3938−3844.
(44) Li, M.-C.; Wu, Q.; Song, K.; Lee, S.; Qing, Y.; Wu, Y. Cellulose Nanoparticles: Structure−Morphology−Rheology Relationships. *ACS Sustainable Chem. Eng.* **2015**, *3*, 821−832.
(45) Nxele, S. R.; Oluwole, D. O.; Nyokong, T. Electrocatalytic Activity of a Push Pull Co(II) Phthalocyanine in the Presence of Graphitic Carbon Nitride Quantum Dots. *Electrochim. Acta* **2019**, *326*, No. 134978.
(46) Lewandowska, A. E.; Eichhorn, S. J. Quantification of the Degree of Mixing of Cellulose Nanocrystals in Thermoplastics Using Raman Spectroscopy. *J. Raman Spectrosc.* **2016**, *47*, 1337−1342.
(47) Gierlinger, N.; Schwanninger, M.; Reinecke, A.; Reinecke, A.; Burger, I. Molecular Changes During Tensile Deformation of Single Wood Fibers Followed by Raman Microscopy. *ACS Biomacromolecules* **2006**, *7*, 2077−2081.
(48) Bovill, A. J.; McConnell, A. A.; Nimmo, J. A.; Smith, W. E. Resonance Raman Spectra of Alpha-Copper Phthalocyanine. *J. Phys. Chem. A* **1986**, *90*, 569−575.

https://doi.org/10.1021/acs.jpcc.2c03531
J. Phys. Chem. C XXXX, XXX, XXX−XXX

(49) Bartholomew, C. R.; McConnell, A. A.; Smith, W. E. Resonance Raman Excitation Profile of Cobalt Phthalocyanine at Room Temperature and 10 K. *J. Raman Spectrosc.* **1989**, *20*, No. 595400.
(50) PaIys, B. J.; Van den Ham, D. M. W.; Briels, W.; Feil, D. Resonance Raman Spectra of Phthalocyanine Monolayers on Different Supports. A Normal Mode Analysis of Zinc Phthalocyanine by Means of the Mndo Method. *J. Raman Spectrosc.* **1995**, 63−76.
(51) McCreery, J. Z. R. L.; McCreery, R. L. Polarized Raman Spectroscopy of Metallophthalocyanine Monolayers on Carbon Surfaces. *Langmuir* **1995**, *11*, 4036−4040.
(52) Tackley, D. R.; Dent, G.; Ewen Smith, W. Ir and Raman Assignments for Zinc Phthalocyanine from Dft Calculations. *Phys. Chem. Chem. Phys.* **2000**, *2*, 3949−3955.
(53) Kumar, A.; Prajapati, P. K.; Aathira, M. S.; Bansiwal, A.; Boukherroub, R.; Jain, S. L. Highly Improved Photoreduction of Carbon Dioxide to Methanol Using Cobalt Phthalocyanine Grafted to Graphitic Carbon Nitride as Photocatalyst under Visible Light Irradiation. *J. Colloid Interface Sci.* **2019**, *543*, 201−213.
(54) Liu, G.; Liu, S.; Lu, Q.; Sun, H.; Xiu, Z. $BiVO_4$/Cobalt Phthalocyanine (CoPc) Nanofiber Heterostructures: Synthesis, Characterization and Application in Photodegradation of Methylene Blue. *RSC Adv.* **2014**, *4*, 53402−53406.
(55) Prajapati, P. K.; Kumar, A.; Jain, S. L. First Photocatalytic Synthesis of Cyclic Carbonates from CO_2 and Epoxides Using COpc/TiO_2 Hybrid under Mild Conditions. *ACS Sustainable Chem. Eng.* **2018**, *6*, 7799−7809.
(56) Guidetti, G.; Atifi, S.; Vignolini, S.; Hamad, W. Y. Flexible Photonic Cellulose Nanocrystal Films. *Adv. Mater.* **2016**, *28*, 10042−10047.
(57) Xu, X.; Liu, F.; Jiang, L.; Zhu, J. Y.; Haagenson, D.; Wiesenborn, D. P. Cellulose Nanocrystals Vs Cellulose Nanofibrils: A Comparative Study on Their Microstructures and Effects as Polymer Reinforcing Agents. *ACS Appl. Mater. Interfaces* **2013**, *5*, 2999−3009.
(58) Lever, A. B. P.; Pickens, S. R.; Minor, P. C.; Licoccia, S.; Ramaswamy, B. S.; Magnell, K. Charge-Transfer Spectra of Metallophthalocyanines-Correlation with Electrode-Potentials. *J. Am. Chem. Soc.* **1981**, *103*, 6800−6806.
(59) Lee, J.; Kim, S. H.; Lee, W.; Lee, J.; An, B. K.; Oh, S. Y.; Kim, J. P.; Park, J. Electrochemical and Optical Characterization of Cobalt, Copper and Zinc Phthalocyanine Complexes. *J. Nanosci. Nanotechnol.* **2013**, *13*, 4338−4341.
(60) Mack, J.; Stillman, M. J. Assignment of the Optical Spectra of Metal Phthalocyanine Anions. *Inorg. Chem.* **1997**, *36*, 413−425.
(61) Wojdyła, M.; Rębarz, M.; Bała, W.; Derkowska, B.; Lukasiak, Z. Optical Properties of Vacuum Sublimed Cobalt Phthalocyanine (CoPc) Thin Layers. *Mol. Cryst. Liq. Cryst.* **2008**, *485*, 974−989.
(62) Marom, N.; Hod, O.; Scuseria, G. E.; Kronik, L. Electronic Structure of Copper Phthalocyanine: A Comparative Density Functional Theory Study. *J. Chem. Phys.* **2008**, *128*, No. 164107.
(63) Böttger, B.; Schindewolf, U.; Möbius, D.; Ávila, J. L.; Martín, M. T.; Rodríguez-Amaro, R. Preparation and Polymorphism of Thin Films of Unsubstituted Cobalt Phthalocyanine. *Langmuir* **1998**, *14*, 5188−5194.
(64) Sharma, A.; Gadly, T.; Gupta, A.; Ballal, A.; Ghosh, S. K.; Kumbhakar, M. Origin of Excitation Dependent Fluorescence in Carbon Nanodots. *J. Phys. Chem. Lett.* **2016**, *7*, 3695−3702.
(65) Spadafora, E. J.; Demadrille, R.; Ratier, B.; Grevin, B. Imaging the Carrier Photogeneration in Nanoscale Phase Segregated Organic Heterojunctions by Kelvin Probe Force Microscopy. *Nano Lett.* **2010**, *10*, 3337−3342.
(66) Matyba, P.; Maturova, K.; Kemerink, M.; Robinson, N. D.; Edman, L. The Dynamic Organic P-N Junction. *Nat. Mater.* **2009**, *8*, 672−676.
(67) Kim, D. Y.; So, F.; Gao, Y. Aluminum Phthalocyanine Chloride/C_{60} Organic Photovoltaic Cells with High Open-Circuit Voltages. *Sol. Energy Mater. Sol. Cells* **2009**, *93*, 1688−1691.
(68) Tietze, M. L.; Tress, W.; Pfützner, S.; Schünemann, C.; Burtone, L.; Riede, M.; Leo, K.; Vandewal, K.; Olthof, S.; Schulz, P.; Kahn, A. Correlation of Open-Circuit Voltage and Energy Levels in Zinc-Phthalocyanine: C_{60} Bulk Heterojunction Solar Cells with Varied Mixing Ratio. *Phys. Rev. B* **2013**, *88*, No. 085119.
(69) Zhang, C.; Keten, S.; Derome, D.; Carmeliet, J. Hydrogen Bonds Dominated Frictional Stick-Slip of Cellulose Nanocrystals. *Carbohydr. Polym.* **2021**, *258*, No. 117682.
(70) Kozub, B. R.; Compton, R. G. Voltammetric Studies of the Redox Mediator, Cobalt Phthalocyanine, with Regard to Its Claimed Electrocatalytic Properties. *Sens. Actuators, B* **2010**, *147*, 350−358.
(71) Bedioui, F.; De Boysson, E.; Devynck, J.; Balkus, K. J. Electrochemical Behaviour of Zeolite-Encapsulated Cobalt Phthalocyanine Complex in DMSO and DMF Solutions. *J. Electroanal. Chem.* **1991**, *315*, 313−318.
(72) Irvine, J. T. S.; Eggins, B. R.; Grimshaw, J. The Cyclic Voltammetry of Some Sulphonated Transition Metal Phthalocyanines in Dimethylsulphoxide and in Water. *J. Electroanal. Chem.* **1989**, *271*, 161−172.
(73) Dong, B.; Fang, Y.; Chen, X.; Xu, H.; Sun, M. Substrate-, Wavelength-, and Time-Dependent Plasmon-Assisted Surface Catalysis Reaction of 4-Nitrobenzenethiol Dimerizing to p,p′-Dimercaptoazobenzene on Au, Ag, and Cu Films. *Langmuir* **2011**, *27*, 10677−10682.
(74) Yang, X.; Yu, H.; Guo, X.; Ding, Q.; Pullerits, T.; Wang, R.; Zhang, G.; Liang, W.; Sun, M. Plasmon-Exciton Coupling of Monolayer MoS_2-Ag Nanoparticles Hybrids for Surface Catalytic Reaction. *Mater. Today Energy* **2017**, *5*, 72−78.
(75) Ding, Q.; Li, R.; Chen, M.; Sun, M. Ag Nanoparticles-TiO_2 Film Hybrid for Plasmon-Exciton Co-Driven Surface Catalytic Reactions. *Appl. Mater. Today* **2017**, *9*, 251−258.
(76) Wu, H.-Y.; Lai, Y.-H.; Hsieh, M.-S.; Lin, S.-D.; Li, Y.-C.; Lin, T.-W. Highly Intensified Surface Enhanced Raman Scattering through the Formation of p,p′-Dimercaptoazobenzene on Ag Nanoparticles/Graphene Oxide Nanocomposites. *Adv. Mater. Interfaces* **2014**, *1*, No. 1400119.
(77) Alam, K. M.; Kumar, P.; Manuel, A. P.; Vahidzadeh, E.; Goswami, A.; Zeng, S.; Wu, W.; Mahdi, N.; Cui, K.; Kobryn, A. E.; et al. CVD Grown Nitrogen Doped Graphene Is an Exceptional Visible-Light Driven Photocatalyst for Surface Catalytic Reactions. *2D Mater.* **2020**, *7*, No. 015002.
(78) Wu, W.; Wu, M.; Sun, Z.; Li, G.; Ma, Y.; Liu, X.; Wang, X.; Chen, X. Morphology Controllable Synthesis of Silver Nanoparticles: Optical Properties Study and Sers Application. *J. Alloys Compd.* **2013**, *579*, 117−123.
(79) Wu, S.; Liu, Y.; Ma, C.; Wang, J.; Zhang, Y.; Song, P.; Xia, L. Effect of Intermolecular Distance on Surface-Plasmon-Assisted Catalysis. *Langmuir* **2018**, *34*, 7240−7247.
(80) Dong, B.; Fang, Y.; Xia, L.; Xu, H.; Sun, M. Is 4-Nitrobenzenethiol Converted to p,p′-Dimercaptoazobenzene or 4-Aminothiophenol by Surface Photochemistry Reaction? *J. Raman Spectrosc.* **2011**, *42*, 1205−1206.
(81) Canpean, V.; Iosin, M.; Astilean, S. Disentangling SERS Signals from Two Molecular Species: A New Evidence for the Production of p,p′-Dimercaptoazobenzene by Catalytic Coupling Reaction of p-Aminothiophenol on Metallic Nanostructures. *Chem. Phys. Lett.* **2010**, *500*, 277−282.
(82) Moskovits, M. Applied Physics. Hot Electrons Cross Boundaries. *Science* **2011**, *332*, 676−677.
(83) Kale, M. J.; Avanesian, T.; Christopher, P. Direct Photocatalysis by Plasmonic Nanostructures. *ACS Catal.* **2014**, *4*, 116−128.
(84) Ding, Q.; Shi, Y.; Chen, M.; Li, H.; Yang, X.; Qu, Y.; Liang, W.; Sun, M. Ultrafast Dynamics of Plasmon-Exciton Interaction of Ag Nanowire- Graphene Hybrids for Surface Catalytic Reactions. *Sci. Rep.* **2016**, *6*, No. 32724.
(85) Cushing, S. K.; Wu, N. Progress and Perspectives of Plasmon-Enhanced Solar Energy Conversion. *J. Phys. Chem. Lett.* **2016**, *7*, 666−75.
(86) Wu, N. Plasmonic Metal-Semiconductor Photocatalysts and Photoelectrochemical Cells: A Review. *Nanoscale* **2018**, *10*, 2679−2696.

https://doi.org/10.1021/acs.jpcc.2c03531
J. Phys. Chem. C XXXX, XXX, XXX−XXX

(87) Cushing, S. K.; Li, J.; Meng, F.; Senty, T. R.; Suri, S.; Zhi, M.; Li, M.; Bristow, A. D.; Wu, N. Photocatalytic Activity Enhanced by Plasmonic Resonant Energy Transfer from Metal to Semiconductor. *J. Am. Chem. Soc.* **2012**, *134*, 15033−41.
(88) Neelgund, G. M.; Oki, A.; Luo, Z. ZnO and Cobalt Phthalocyanine Hybridized Graphene: Efficient Photocatalysts for Degradation of Rhodamine B. *J. Colloid Interface Sci.* **2014**, *430*, 257−64.
(89) Chen, W.; Lu, W.; Yao, Y.; Xu, M. Highly Efficient Decomposition of Organic Dyes by Aqueous-Fiber Phase Transfer and In Situ Catalytic Oxidation Using Fiber-Supported Cobalt Phthalocyanine. *Environ. Sci. Technol.* **2007**, *41*, 6240−5.
(90) Çakır, V.; Saka, E. T.; Bıyıklıoğlu, Z.; Kantekin, H. Highly Selective Oxidation of Benzyl Alcohol Catalyzed by New Peripherally Tetra-Substituted Fe(II) and Co(II) Phthalocyanines. *Synth. Met.* **2014**, *197*, 233−239.
(91) Wang, R.-M.; Wang, H.; Wang, Y.; Li, H.-R.; He, Y.-F.; Hao, E.-X. Preparation and Photocatalytic Activity of Chitosan-Supported Cobalt Phthalocyanine Membrane. *Color. Technol.* **2014**, *130*, 32−36.
(92) Marinescu, C.; Ben Ali, M.; Hamdi, A.; Cherifi, Y.; Barras, A.; Coffinier, Y.; Somacescu, S.; Raditoiu, V.; Szunerits, S.; Boukherroub, R. Cobalt Phthalocyanine-Supported Reduced Graphene Oxide: A Highly Efficient Catalyst for Heterogeneous Activation of Peroxymonosulfate for Rhodamine B and Pentachlorophenol Degradation. *Chem. Eng. J.* **2018**, *336*, 465−475.
(93) Hu, X.; Mohamood, T.; Ma, W.; Chen, C.; Zhao, J. Oxidative Decomposition of Rhodamine B Dye in the Presence of VO_2+ and/or Pt(IV) under Visible Light Irradiation: *N*-Deethylation, Chromophore Cleavage, and Mineralization. *J. Phys. Chem. B* **2006**, *110*, 26012−26018.
(94) Zhao, N.; Peng, J.; Liu, G.; Zhang, Y.; Lei, W.; Yin, Z.; Li, J.; Zhai, M. PVP-Capped CdS Nanopopcorns with Type-II Homojunctions for Highly Efficient Visible-Light-Driven Organic Pollutant Degradation and Hydrogen Evolution. *J. Mater. Chem. A* **2018**, *6*, 18458−18468.
(95) Kumar, P.; Vahidzadeh, E.; Thakur, U. K.; Kar, P.; Alam, K. M.; Goswami, A.; Mahdi, N.; Cui, K.; Bernard, G. M.; Michaelis, V. K.; Shankar, K. C_3N_5: A Low Bandgap Semiconductor Containing an Azo-Linked Carbon Nitride Framework for Photocatalytic, Photovoltaic and Adsorbent Applications. *J. Am. Chem. Soc.* **2019**, *141*, 5415−5436.
(96) Alam, K. M.; Jensen, C. E.; Kumar, P.; Hooper, R. W.; Bernard, G. M.; Patidar, A.; Manuel, A. P.; Amer, N.; Palmgren, A.; Purschke, D. N.; et al. Photocatalytic Mechanism Control and Study of Carrier Dynamics in CdS@C_3N_5 Core−Shell Nanowires. *ACS Appl. Mater. Interfaces* **2021**, *13*, 47418−47439.
(97) Zhuang, J.; Dai, W.; Tian, Q.; Li, Z.; Xie, L.; Wang, J.; Liu, P.; Shi, X.; Wang, D. Photocatalytic Degradation of RhB over TiO_2 Bilayer Films: Effect of Defects and Their Location. *Langmuir* **2010**, *26*, 9686−94.
(98) Haldar, S.; Bhandary, S.; Vovusha, H.; Sanyal, B. Comparative Study of Electronic and Magnetic Properties of Iron and Cobalt Phthalocyanine Molecules Physisorbed on Two-Dimensional MoS_2 and Graphene. *Phys. Rev. B* **2018**, *98*, No. 085440.
(99) de Silva, P.; Corminboeuf, C. Simultaneous Visualization of Covalent and Noncovalent Interactions Using Regions of Density Overlap. *J. Chem. Theory Comput.* **2014**, *10*, 3745−3756.
(100) Bregado, J. L.; Secchi, A. R.; Tavares, F. W.; de Sousa Rodrigues, D.; Gambetta, R. Amorphous Paracrystalline Structures from Native Crystalline Cellulose: A Molecular Dynamics Protocol. *Fluid Phase Equilib.* **2019**, *491*, 56−76.
(101) Liao, M.-S.; Scheiner, S. Electronic Structure and Bonding in Metal Phthalocyanines, Metal = Fe, Co, Ni, Cu, Zn, Mg. *J. Chem. Phys.* **2001**, *114*, 9780−9791.
(102) Matunová, P.; Jirasek, V.; Rezek, B. Dft Calculations Reveal Pronounced Homo-Lumo Spatial Separation in Polypyrrole-Nanodiamond Systems. *Phys. Chem. Chem. Phys.* **2019**, *21*, 11033−11042.
(103) Li, H.; Chi, Z.; Xu, B.; Zhang, X.; Yang, Z.; Li, X.; Liu, S.; Zhang, Y.; Xu, J. New Aggregation-Induced Emission Enhancement Materials Combined Triarylamine and Dicarbazolyl Triphenylethylene Moieties. *J. Mater. Chem.* **2010**, *20*, 6103−6110.
(104) Zeman, E. J.; Carron, K. T.; Schatz, G. C.; Van Duyne, R. P. A Surface Enhanced Resonance Raman Study of Cobalt Phthalocyanine on Rough Ag Films: Theory and Experiment. *J. Chem. Phys.* **1987**, *87*, 4189−4200.
(105) Atef Gadalla, J.-B. B.; Bowen, M.; Boukari, S.; Beaurepaire, E.; Crégut, O.; Gallart, M.; Hönerlage, B.; Gilliot, P. Ultrafast Optical Dynamics of Metal-Free and Cobalt Phthalocyanine Thin Films. *J. Phys. Chem. C* **2010**, *114*, 17854−17863.
(106) Yan, Y.; Lu, S.; Li, B.; Zhu, R.; Zhou, J.; Wei, S.; Qian, S. Ultrafast Excited State Dynamics of Modified Phthalocyanines: P-Hpczn and P-Hpcco. *J. Phys. Chem. A* **2006**, *110*, 10757−62.

https://doi.org/10.1021/acs.jpcc.2c03531
J. Phys. Chem. C XXXX, XXX, XXX−XXX